THE ASTROPHYSICAL JOURNAL, 331:435–462, 1988 August 1

SPECTRAL EVOLUTION OF ASYMPTOTIC GIANT BRANCH STARS[1]

KEVIN VOLK AND SUN KWOK
Department of Physics, The University of Calgary
Received 1987 June 17; accepted 1988 January 25

ABSTRACT

The evolution of the infrared spectra of asymptotic giant branch (AGB) stars has been obtained by time-dependent radiative transfer models. Based on a simple mass-loss formula, the evolution of intermediate mass stars on the AGB has been calculated. The results of these models are compared with the photometric and spectroscopic observations of AGB stars by the *IRAS* satellite. Due to the availability of a large uniform sample of high-quality data, we are able to critically test the formula of mass loss for AGB stars. The present mass-loss formula suggests that AGB stars with the 10 μm silicate feature in absorption are mostly stars with main-sequence masses higher than 3 $M_\odot$.

Subject headings: infrared: spectra — radiative transfer — stars: circumstellar shells — stars: evolution — stars: late-type — stars: mass loss

I. INTRODUCTION

The 10 μm silicate dust feature associated with late-type stars was discovered by Woolf and Ney (1969). It was later established that this feature is commonly present in oxygen-rich stars with spectral types later than M3 (Gehrz and Woolf 1971) and is a manifestation of mass loss during the asymptotic giant branch (AGB) evolution. Unlike its counterpart in carbon-rich stars—the 11.2 μm silicon carbide dust feature—the silicate feature is observed both in emission and in self-absorption, suggesting a wide range of 10 μm optical depths in the circumstellar envelope (Merrill and Stein 1976). The change in optical thickness has been interpreted as a result of the increasing mass-loss rate from the underlying stars as they evolve up the AGB (Merrill 1977).

The 10 μm silicate feature has also been observed in many infrared stars discovered in the 2 μm sky survey (Neugebauer and Leighton 1969), the AFGL infrared sky survey (Walker and Price 1975), and OH surveys (Johansson *et al.* 1977; Baud *et al.* 1979). Since many of these infrared stars have no optical counterparts, they are likely to be late AGB stars completely surrounded by and obscured by circumstellar dust. As the direct observation of the photosphere is a difficult, if not impossible, task, spectroscopic observations of the circumstellar envelope represents the only avenue to infer the evolutionary status of the central stars. The density profile, and therefore the mass-loss rates, can in principle be derived from an analysis of the infrared spectra and dust feature strengths of the circumstellar emission. Many model calculations employing the techniques of continuum radiation transfer have been performed in the past, providing information on both the silicate dust opacity function and the circumstellar density structure (Jones and Merrill 1976; Taam and Schwartz 1976; Crabtree and Martin 1979; Rowan-Robinson and Harris 1983*a*, *b*). However, one limitation of all the previous models is that they are static models, assuming a fixed luminosity, temperature, and mass-loss rate of the central stars without taking into account the rapidly evolving nature of AGB stars.

It is now believed that intermediate mass ($<8\ M_\odot$) stars evolve up the AGB in less than 10^7 yr. During this short period, the stellar luminosity can increase by up to a factor of 10, the effective temperature decreases by a factor of 2, and the mass-loss rate increases by up to 3 orders of magnitude (cf. Kwok 1987). The structure of the circumstellar envelope, with a dynamic time scale of $\sim 10^5$ yr, will likely reflect the changing nature of the central star. The time-dependent nature is particularly dramatic in the latest part of AGB evolution, where the stars are evolving extremely rapidly. It is therefore highly desirable to attempt time-dependent models where the radiative transfer calculations on the circumstellar envelope are coupled with an evolving model of the central star.

One study which incorporates the time-dependent nature of AGB mass loss is that of Bedijn (1986, 1987), in which the infrared photometric colors of a sample of Mira variables and OH/IR stars observed with the *Infrared Astronomical Satellite* (*IRAS*) are used as comparison data for a set of radiative transfer models. These models were done assuming that an AGB star evolves at constant temperature and luminosity while its mass-loss rate continuously increases. By comparing the model colors to the observations Bedijn concludes that a mass-loss formula

$$\dot{M} = \dot{M}_0(1 - t/\tau)^{-1} \quad t < \tau\ ,\ \tau = \text{constant} \qquad (1)$$

is able to fit the data. This "accelerated mass-loss formula" is assumed by Bedijn to apply to the last 10^5 yr of the AGB evolution. One drawback of Bedijn's model is the assumption that the stellar radius will remain constant as the stellar wind removes large amounts of material from the stellar envelope. Nevertheless Bedijn was able to use this formula to reproduce the color changes of OH/IR stars as they evolve up the AGB.

There is no doubt that the mass loss plays an important role in the evolution of AGB stars. The observed $\dot{M}$ values are usually at least as large as the estimated rate of change in the mass of the stellar core due to the shell nuclear reactions. In the cases where the stellar wind exceeds $\dot{M} \approx 10^{-6}\ M_\odot\ \text{yr}^{-1}$ the mass loss will dominate the stellar evolution. It is therefore important to obtain a self-consistent model where both the effects of mass loss and nuclear burning are considered. In this paper, we will attempt to calculate the evolution of the spectra of the circumstellar envelope of AGB stars as a function of time and initial mass. By assuming mass-loss formulae in parameterized form, the computed emergent spectra are compared

[1] *Pub. Rothney Ap. Obs., No. 49.*

with spectra of AGB stars obtained by the *IRAS* satellite. Using the spectra and colors of *IRAS* AGB stars as observational constraints, we hope to obtain a more realistic empirical formula of mass loss.

II. THE *IRAS* DATA

The *Infrared Astronomical Satellite* was launched in 1983, with the purpose of carrying out a survey of the sky in the middle-to far-infrared from space. Over the 10 month lifetime of the satellite, *IRAS* surveyed 96% of the sky using medium-band infrared photometry at wavelengths of 12, 25, 60 and 100 μm. Over 245,000 point sources were identified in the course of the survey. At the same time a low-resolution spectrometer ($\lambda/\Delta\lambda \approx 40$) covering the wavelength range from 7.7 to 22.6 μm was in operation, providing the spectra of the brighter point sources. The satellite is described by Pouw (1983) while details of the data processing and the characteristics of the various catalogs produced from the *IRAS* data are given in the *IRAS Explanatory Supplement* (1985). A total of 5425 spectra were obtained by *IRAS* to form the *Catalog of Low Resolution Spectra* (LRSC, 1986). Out of the 5425 spectra, 2113 show the 10 μm silicate dust feature. This group of objects includes both emission and absorption feature sources, indicating a wide range of dust optical depths in the sample. Although some of these objects are associated with early-type stars embedded in interstellar dust, H II regions, and sources in star-formation regions, most of them are expected to be intermediate-mass AGB stars.

Each LRSC spectra was assigned a two-digit classification number based upon features seen in the spectrum. Those LRSC classes which are for silicate feature objects are as follows.

1. LRSC class 20–29: 1738 objects which show the 10 μm feature in emission and which have a "blue" continuum, identified by the *IRAS Explanatory Supplement* with M stars with dust envelopes:

2. LRSC class 30–39: 230 objects which show the 10 μm feature in absorption and which have a "blue" continuum, identified with M stars with thicker dust envelopes than the class 20s;

3. LRSC class 60–69:78 objects which show the 10 μm feature in emission and which have a "red" continuum, identified with M stars having still thicker dust envelopes than the previous two groups;

4. LRSC class 70–79:67 objects which show the 10 μm feature in absorption and which have a "red" continuum, identified with stars having the thickest dust envelopes of all the objects showing the 10 μm feature in the spectrum.

The "red" continuum or "blue" continuum classification is based upon the spectral index between 15 and 22 μm in the spectrum obtained by *IRAS*. If the λF_λ value rises between 22 and 15 μm the spectrum is said to be "red," else it is said to be "blue." Within each group, the second digit represents the strength of the feature with a larger number inferring a stronger feature. The *IRAS* subclass from 1 to 9 is approximate; a better estimate of the feature strength can be obtained by fitting the continuum as in Volk and Kwok (1987).

The LRSC class identifications given in the *IRAS Explanatory Supplement* is not flawless. It is now known that some of the class 31 to 39 (hereafter referred to as class 30 objects) as well as class 71 to 79 (hereafter class 70) objects are confused with H II regions showing the 10 μm feature in absorption. The class 30s also contain K-type or earlier type stars, with local circumstellar dust from a molecular cloud causing the feature.

Within the four groups of objects which show the silicate dust feature, there is a clear evolutionary trend for the class 20 and class 30 objects based upon the properties of the objects. The color temperature of these objects declines as the silicate feature changes from emission to absorption (Volk and Kwok 1987) for the "blue" objects. The class 70 objects have even lower color temperatures than the strongest class 39 objects, usually near 100 K. On that basis they appear to be more extreme cases of silicate absorption than the class 30 objects. The only group for which interpretation is difficult is the class 60 objects, because the redness of the spectrum implies that they have a fairly high dust optical depth so as to reduce the temperature of the radiating surface, while the feature appears in emission thus implying a low optical depth. The nature of the class 60 objects is the subject of another paper (Volk and Kwok 1988).

a) The Working Sample

Out of the 2113 silicate feature objects in the LRSC a subset of 467 objects was chosen on the basis of their having good quality photometric data at all four wavelengths observed by *IRAS*. This group of objects (hereafter referred to as the working sample) forms the observational database for comparison with our theoretical models. The requirement of four good fluxes will likely eliminate any stars of comparatively early spectral types, which would be weak at 100 μm, as well as distant objects.

The 467 objects in the working sample break down into 179 of classes 21 to 24, 196 of classes 25 to 29, 38 of classes 31 to 39, 14 of classes 61 to 69, and 40 of classes 71 to 79. Compared with the entire sample, the working sample contains slightly less of the class 31 to 39 and class 61 to 69 objects than would be expected. The most significant distinction between the working sample and the complete sample is that there is a much lower proportion of class 25 to 29 objects in the working sample. Out of the 1732 class 21 to 29 objects 488 are of classes 21 to 24, and the remaining 1244 are of classes 25 to 29. In choosing the working sample, only 16% of the stronger emission feature objects (class 25 to 29) were included. This indicates that the stronger emission feature objects are less luminous on the average than those with weaker emission features and thus are not observed over as large a volume of space. Such a trend can be understood if the class 21 to 24 objects are more likely to be objects where the emission feature is declining in strength as the dust optical depth increases and the feature is becoming an absorption feature rather than objects with very low dust optical depths. If this is true then the average class 21 to 24 object is actually further evolved on the AGB than the average class 25 to 29 object.

b) Color Distributions

The properties of the various classes are best illustrated by plotting the *IRAS* photometry values in the form of color-color diagrams. Figures 1 and 2 show respectively the 12/25/60 and 25/60/100 color-color diagrams of the working sample. Figure 1 shows a clear separation of the different classes of spectra except for the class 60 objects. The class 21 to 29 objects form a tight group in the lower left corner of the 12/25/60 μm color-color diagram. The class 25 to 29 objects appear to show more scatter than the class 21 to 24 objects, while the class 21 to 24 objects show some tendency to be centered to the

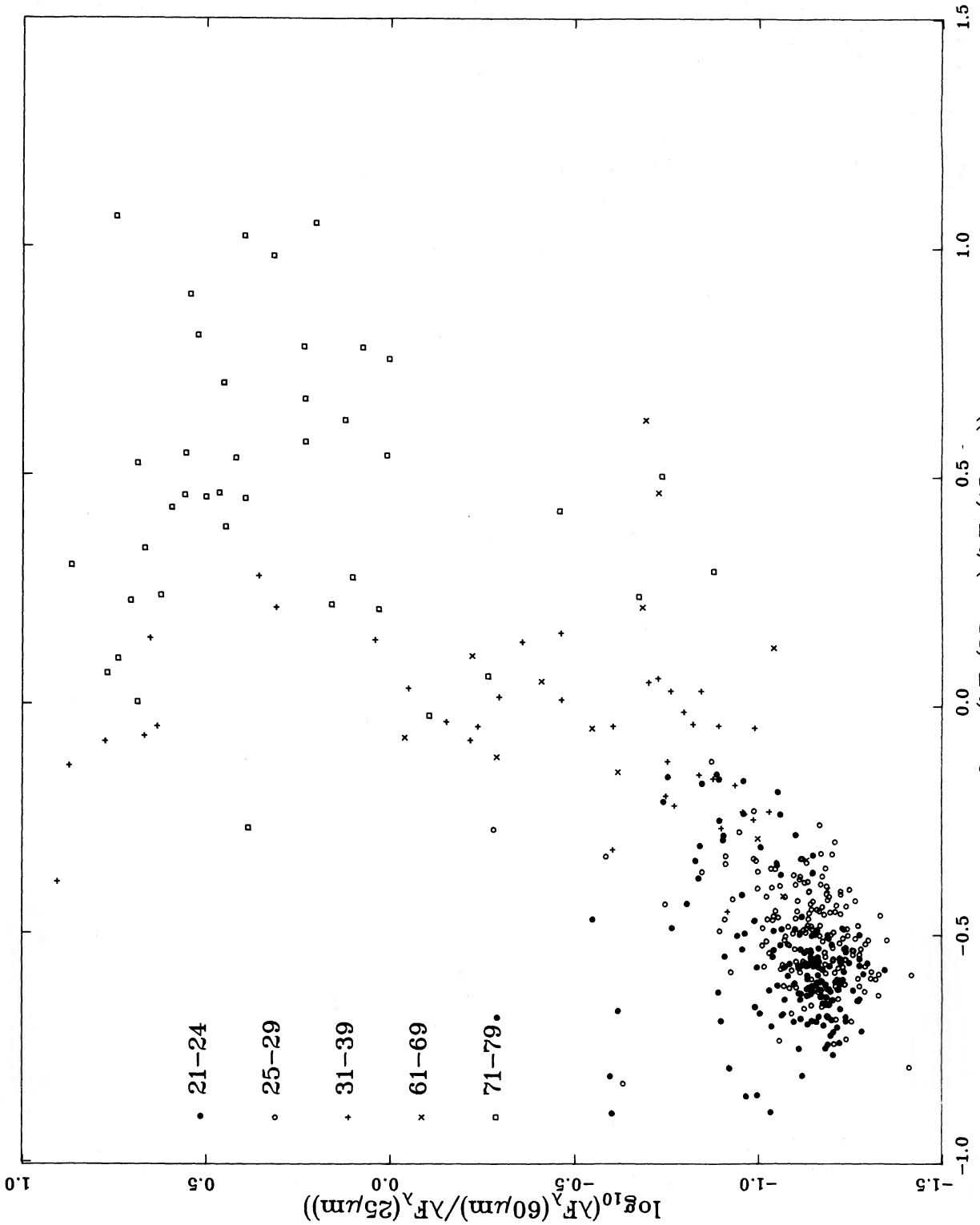

FIG. 1.—The 12/25/60 μm color-color diagram for the 467 stars in the working sample

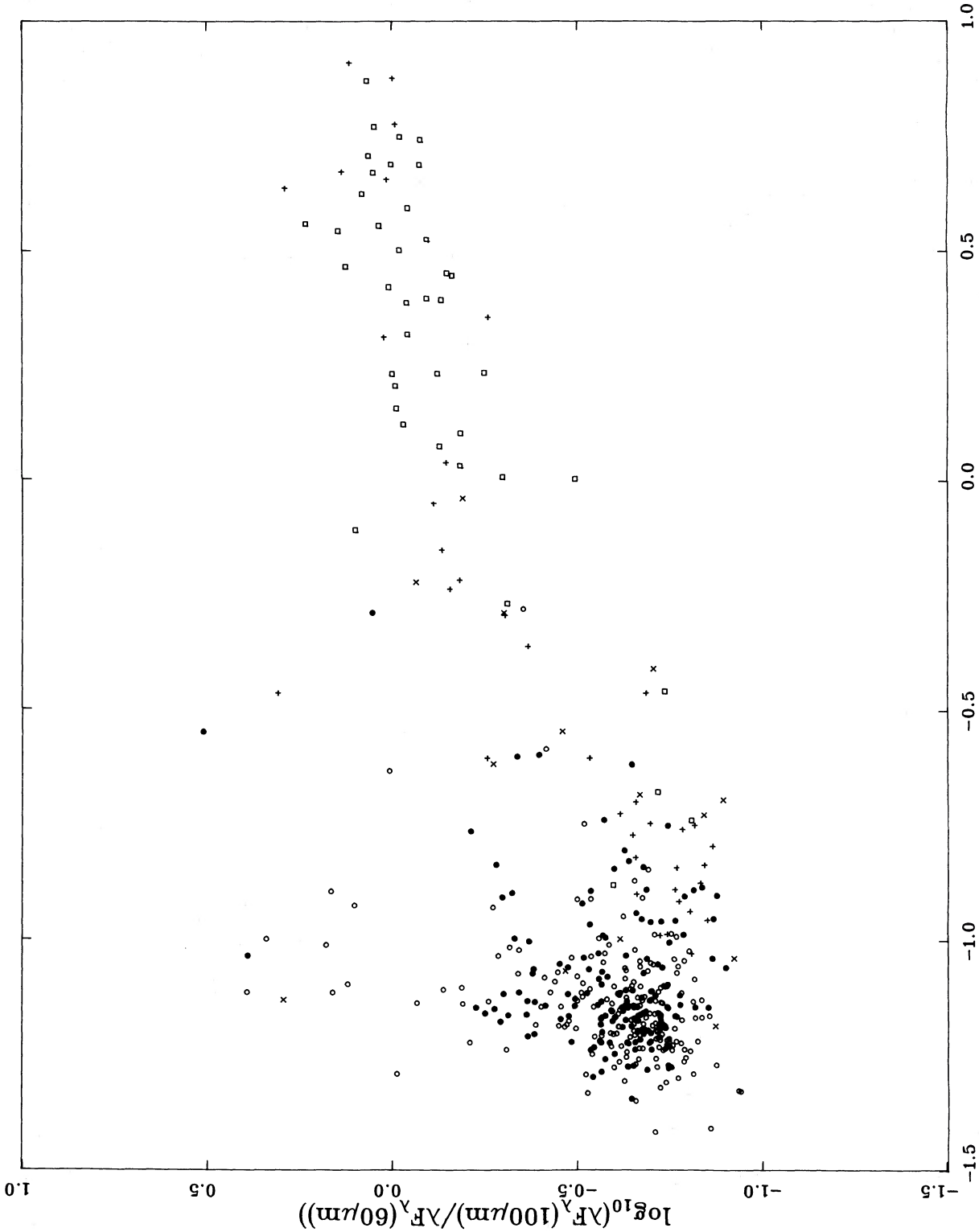

FIG. 2.—The corresponding 25/60/100 μm color-color diagram for the sources in the working sample. The symbols are the same as in the legend of Fig. 1.

right of the class 25 to 29 objects. These tendencies are not strong; at any point in the area where the class 20 are congregated one typically finds objects with a wide range of 10 μm feature strengths.

Class 30 objects generally occupy an area to the upper right of the class 20 objects. This indicates a lower temperature for these sources and suggests an evolution from the lower left corner up through the middle of the color-color diagram as the dust optical depth becomes larger. There are a few unusual class 30 sources which are found near the top center of Figure 1, some of which turn out to be associated with H II regions. These sources are probably not AGB stars and will be ignored in the following discussions.

The class 70 objects are found in the upper right area of the color-color diagram and are generally separated from the class 30 objects. All of these objects are very red. A few of them are situated to the right of the main group of class 31 to 39 objects, while most of them are found higher in the diagram with $\log_{10}$ $[\lambda F_\lambda(60\ \mu\text{m})/\lambda F_\lambda(25\ \mu\text{m})] > 0$. About 40% of the class 70 objects are associated with H II regions; it may be that none of them are AGB stars. Figure 1 seems to suggest a continuous evolution from the class 20s to the class 70s along an "S" shaped curve. However, in view of the degree of confusion among class 70 objects, we doubt that the AGB in fact extends to the upper part of Figure 1.

The class 60 objects in Figure 1 do not form a group. Some of them are found in the same area as the class 21 to 29 objects. For these sources inspection of the spectra shows that they are actually strong emission feature objects for which the 18 μm silicate feature is rather weak for some reason, leading to flat spectra from 15 to 22 μm. This accounts for four of the 14 class 60 objects in the working sample and a similar fraction of all the class 60 sources. The remaining sources do not form a homogeneous group either in colors or in the characteristics of the spectra and their nature is uncertain.

Figure 2 shows the 25/60/100 μm color-color diagram for the working sample. We can see that the class separations are not as strong in Figure 2 as in Figure 1. There is a clear separation of the class 21 to 29 objects from the absorption feature objects. The class 20 objects form a group at the center left of the diagram, separated from the absorption objects (classes 30 and 70) to the right. Overall there is not that much change in the $\log_{10}$ $[\lambda F_\lambda(100\ \mu\text{m})/\lambda F_\lambda\ (60\ \mu\text{m})]$ value for most of the objects although the value does increase somewhat as one considers the absorption objects. The general trend is a more or less linear path from left to right in Figure 2, sloping upward slightly.

One feature of Figure 2 is that there are a number of class 20 sources which have significant 100 μm excesses, larger by up to a factor of 10 than the main group of objects. An examination of these anomalous sources shows that many of them suffer from cirrus contamination. The 100 μm fluxes are therefore not reliable. A number of objects in Figure 1 also show 60 μm excesses in comparison with the majority of class 20 objects. Some of these sources are identified as carbon stars and not oxygen-rich objects. The nature of these objects is discussed in a separate paper (Chan and Kwok 1988).

There is also a tendency for the class 30 objects to lie to the left of the class 70 objects in Figure 2. By comparing Figures 1 and 2 it appears that the class 30 objects found furthest right in Figure 2 are those which are situated at the top of Figure 1 and which tend to be associated with H II regions. There is a suggested division in Figure 2 around $\log_{10}$ $[\lambda F_\lambda(60\ \mu\text{m})/\lambda F_\lambda\ (25\ \mu\text{m})] = -0.3$ which may separate the H II region sources from the AGB stars.

c) *Comparison with OH/IR Stars*

OH/IR stars have been widely suggested to be late AGB stars and therefore should have similar properties to the stars in our working sample. In Figure 3 we show the color-color

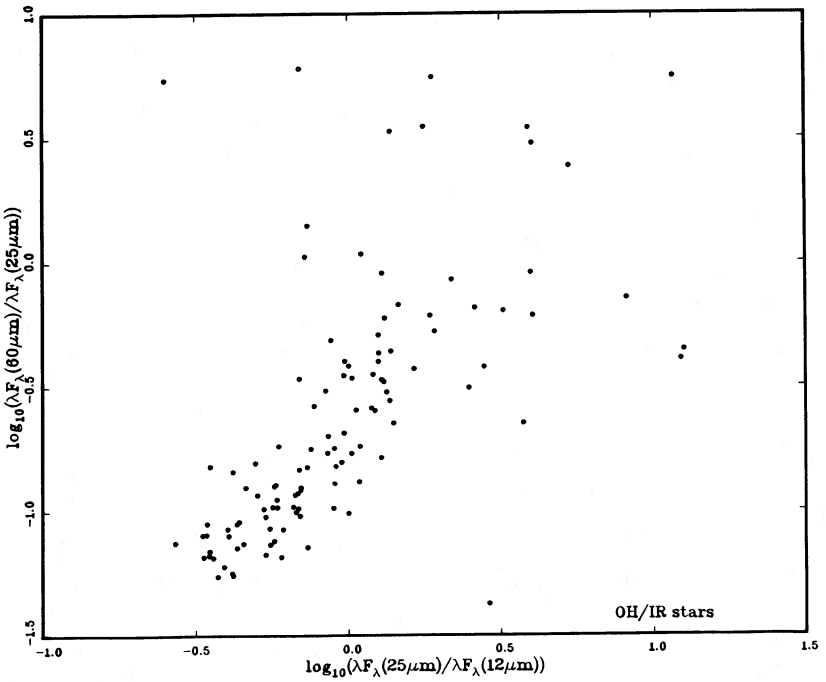

FIG. 3.—The color-color diagram for 100 OH/IR stars which are also sources in the *IRAS* Point Source Catalog. Most of the OH/IR stars with $\log_{10}$ $[\lambda F_\lambda(60\ \mu\text{m})/\lambda F_\lambda(25\ \mu\text{m})] > +0.2$ are believed to be contaminated by H II regions.

diagram of 100 OH/IR stars which have positional coincidence with *IRAS* sources. A few objects are members of the working sample. The OH/IR stars have a very similar distribution on the color-color diagram as the 467 silicate feature objects, except that only a few OH/IR stars are found in the area belonging to the class 20 objects. This probably implies that the OH maser emission does not appear until the circumstellar envelope is dense enough to saturate the maser. Most of the OH/IR stars fall in the area of the color-color diagram populated by class 30 objects with some overlapping with class 70 objects. The only major difference between Figures 1 and 3 is that in Figure 3 there are a significant number of objects with $\log_{10}[\lambda F_\lambda(25\ \mu m)/\lambda F_\lambda(12\ \mu m)] > 0.1$ and $\log_{10}[\lambda F_\lambda(60\ \mu m)/\lambda F_\lambda(25\ \mu m)] < 0$ where very few sources are found in Figure 1. These sources are generally nonvariable OH/IR stars according to Olnon *et al.* (1984) and they are interpreted by Bedijn (1987) as post-AGB stars in which circumstellar shells are detached from the stars themselves. If this is the case then the duration of the phase is expected to be short which may explain why such stars are rare in the LRSC sample.

Figure 3 also shows several OH/IR stars with very red colors ($\log_{10}[\lambda F_\lambda(60\ \mu m)/\lambda F_\lambda(25\ \mu m)] > +0.2$) which are not plotted in Figure 2 of Olnon *et al.* (1984). These stars occupy the same area as the class 70 LRSC objects. Many of the type 70 LRSC objects have associations with H II regions, and of the nine OH/IR stars near the top of Figure 3 five have associations with H II regions. One of the others is associated with an OB association. The other three have no associations according to *IRAS* and could be more distant than those with associations as they have lower infrared flux values. Thus it appears that all the sources in this area of the color-color diagram are actually contaminated by low-temperature interstellar dust emissions.

There are also a few OH/IR stars which are not AGB stars (e.g., VY CMa) but He-core burning supergiants (Jones 1987). These stars are discussed in the next section.

As for the 25/60/100 μm color-color diagram, there are only a few OH/IR stars which have good 100 μm photometry data and no definite conclusion can be drawn. Those OH/IR stars for which 100 μm measurement is available appear to be distributed similarly to the class 30 objects in Figure 2.

d) Supergiants

Another question to consider is whether the working sample is contaminated by the presence of core-burning massive ($>8\ M_\odot$) stars. A search for two supergiants with large infrared excess (VY CMa and VX Sgr) in the LRSC showed that these objects have the 10 μm feature in emission rather than absorption. Their *IRAS* identifications are respectively 07209−2540 (class 24) and 18050−2213 (class 26). These stars appear to be indistinguishable from the bulk of LRSC class 20 objects. Assuming that these two objects are typical of supergiants which have been observed by *IRAS*, they do not have a major effect on the color distribution of AGB stars.

e) Variability

AGB stars are known to be radial pulsators with periods of several hundred days (Wood and Cahn 1977; Feast 1986). Monitoring of OH and infrared variations in OH/IR stars suggest periods as long as 2000 days (Engels *et al.* 1985; Herman and Habing 1985). There are, however, some OH/IR stars which show no variability and these nonvariable OH/IR stars have been suggested to be stars which have evolved beyond the AGB (Bedijn 1987). Two passes of the *IRAS* survey are separated by 6 months and the comparison of the fluxes allow the assessment of the likelihood of variability. This was expressed as a % variability value in the *IRAS* Point Source Catalog.

Examination of the variability data for the working sample shows that the variability of the objects does tend to decline with increasing optical depth of the dust shells. One hundred and thirteen of the 182 objects of classes 25 to 29 have an *IRAS* % variability of more than 75%, values high enough to strongly imply variability, compared with 42 of the 162 class 21 to 24 objects, 16 of the 36 class 31 to 39 objects, one of the 12 class 61 to 69 objects, and four of the 36 class 71 to 79 objects. In each group there are some objects for which no % variability value was assigned. Assuming that the evolution will proceed from the upper class 20s to the lower class 20s and on to the class 30s as the optical depth of the dust increases, these values are consistent with a decline in the variability. One must be cautious about this conclusion because the *IRAS* observations are best suited to detect periods of 200 to 400 days but may have been too closely spaced to detect long-period variations.

f) Galactic Distribution

Another approach to study the nature of these objects is to examine their galactic distribution. The galactic distributions of the class 20, 30, 60, and 70 objects are shown in Figures 4 to 7, respectively. For the last three groups the positions of all the sources are plotted while for the class 21 to 29 objects only the members of the working sample are plotted due to the large number of objects of this class. Figures 4 and 5 suggest that the class 21 to 29 objects are generally nearby (<2 kpc) objects because they are commonly seen at high galactic latitudes. The class 30 objects are clustered much closer to the galactic plane and thus are more distant or have more massive progenitors than the class 20 objects. The class 70 objects show the distribution closest to the galactic plane, consistent with their being sources associated with H II regions.

Habing *et al.* (1985) have shown that the late-type star population in the *IRAS* Point Source Catalog exhibits a very prominent galactic bulge. In comparison, the galactic distribution of the sources in our working sample shows no sign of the bulge. In fact, a plot of the galactic distribution of all sources in the LRSC fails to show the galactic bulge. This most natural explanation is that the stars in the LRSC, and our working sample in particular, belong to a relatively local population. Comparison of the 12 μm flux values ($\sim$4 Jy) of bulge stars with the limiting 12 μm flux ($\sim$10 Jy) that allows a source to be admitted to the LRSC suggests that the LRSC sources are limited to within a distance of 5–6 kpc. Since one of the requirements of our working sample is a good 100 μm flux, the average distance of sources in the working sample must be even smaller.

In summary, we conclude that most of the sources in the LRSC class 20 objects are AGB stars, although the second digit of the classification is not necessarily an indication of the star's evolutionary status. We also conclude that the class 30 objects as a group are more evolved than the class 20 objects. The class 30 objects, however, suffers from confusion with H II regions and we believe that most of the sources with $\log_{10}[\lambda F_\lambda(60\ \mu m)/\lambda F_\lambda(25\ \mu m)] > -0.3$ are not AGB stars. The nature of class 60 objects is not clear and very few of the class 70 objects are AGB stars. We will therefore exclude these two classes from our following discussions.

III. MATHEMATICAL FORMULATION OF THE MODEL

Discussions in the previous section demonstrate that the *IRAS* survey has provided us with a large sample of uniformly

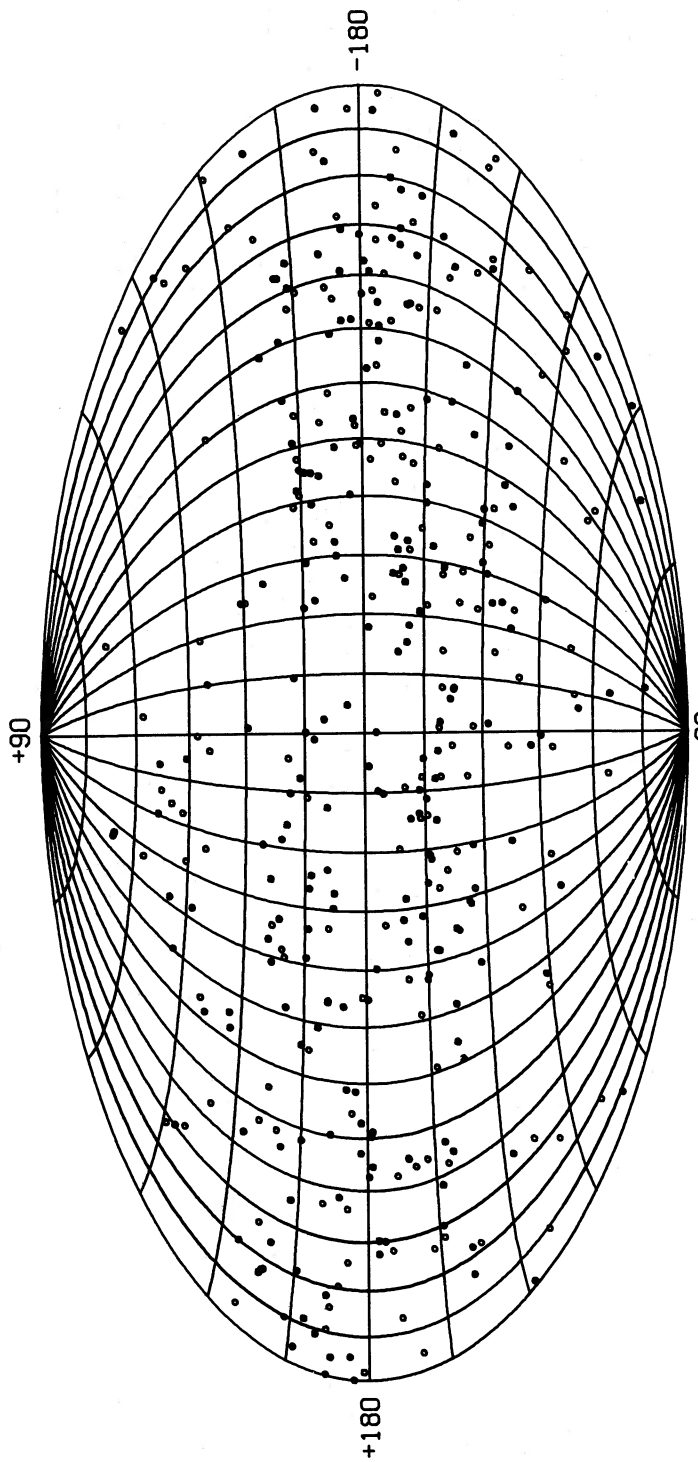

FIG. 4.—The galactic distribution of the LRSC class 20 sources in the working sample. The LRSC 20–24 objects are shown as open circles and LRSC 25–29 objects as filled circles.

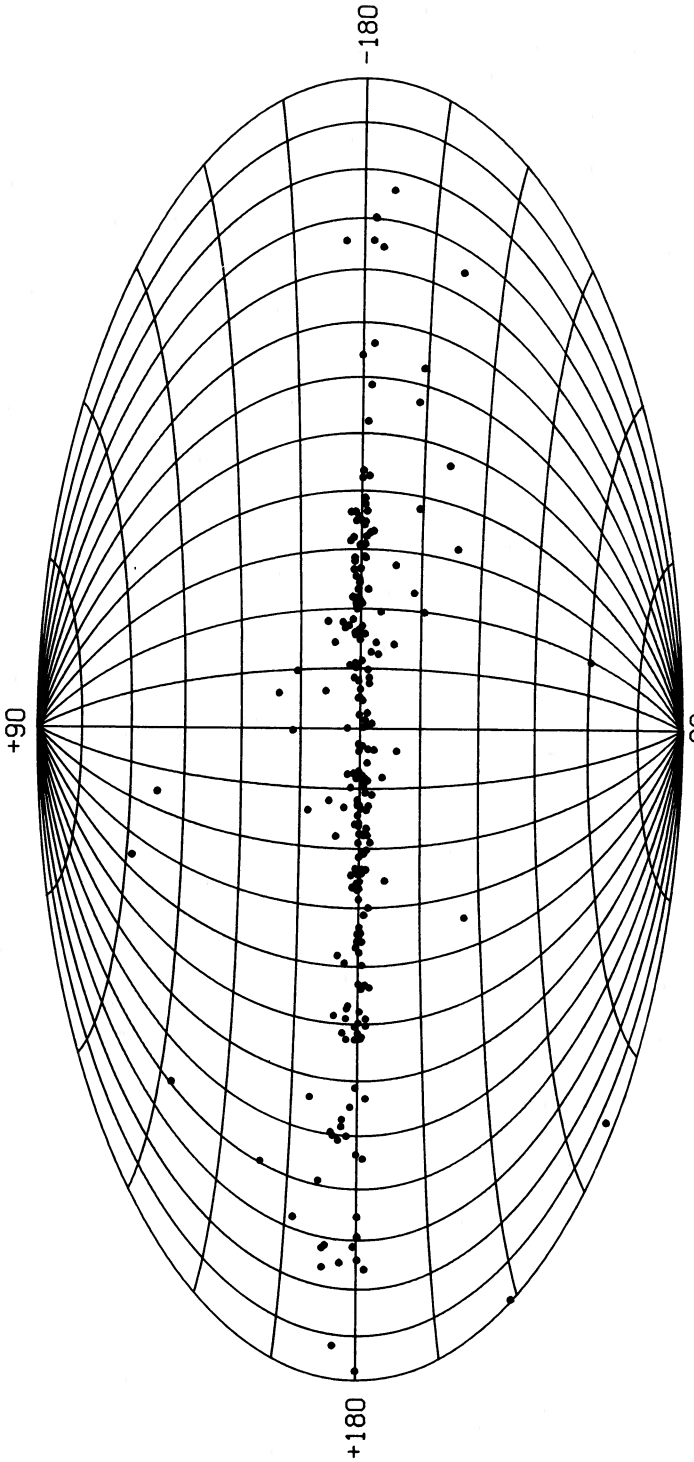

FIG. 5.—The galactic distribution of the class 30 sources in the LRSC

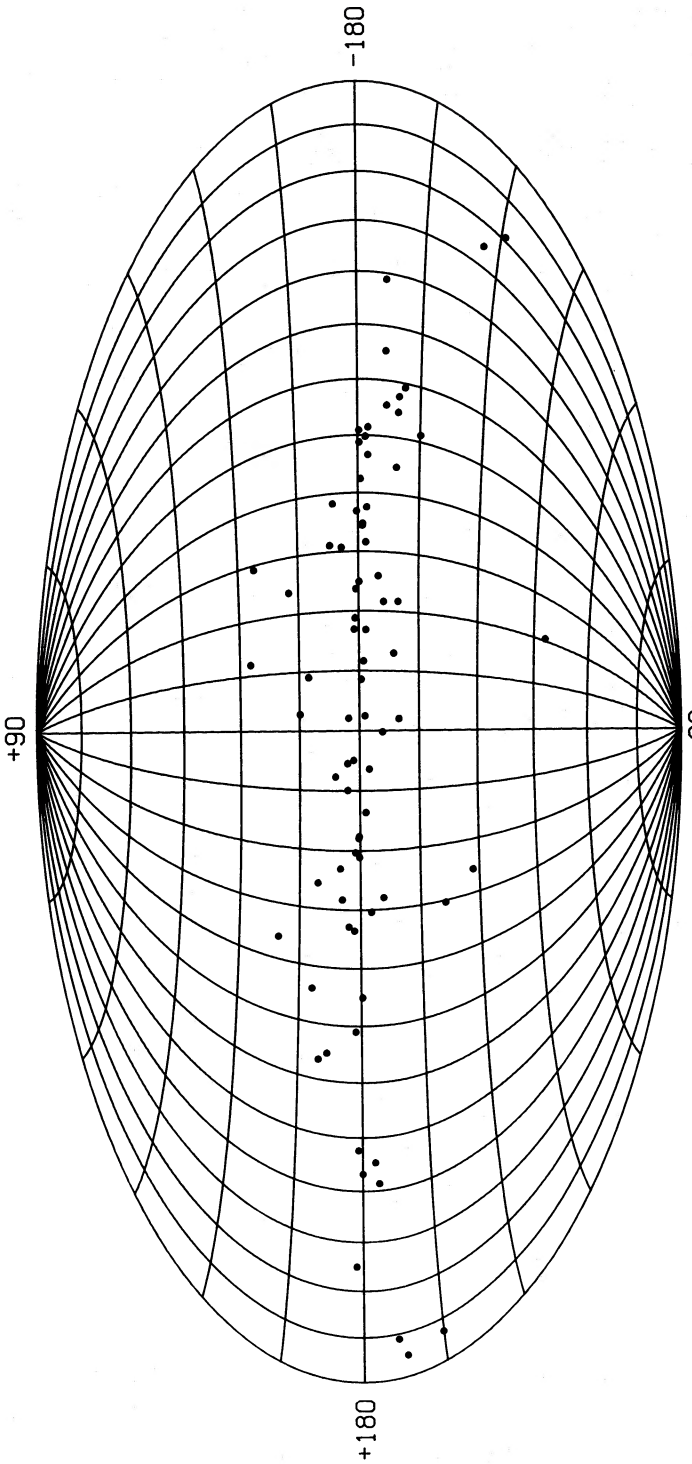

FIG. 6.—The galactic distribution of the class 60 sources in the LRSC

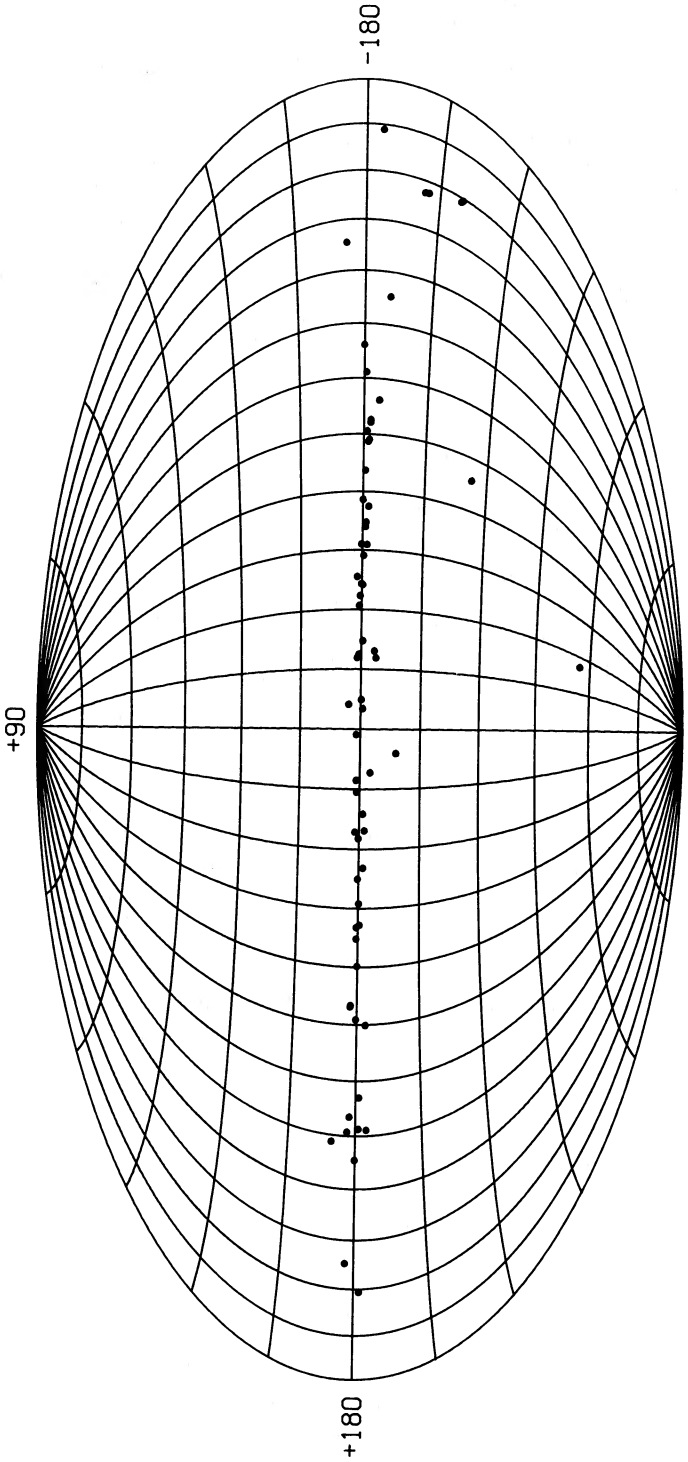

FIG. 7.—The galactic distribution of the class 70 sources in the LRSC

high-quality data on AGB and late AGB stars. In particular, observations by the low resolution spectrometer have produced detailed spectra of the 10 and 18 μm features of the circumstellar silicate dust which evolves as the star ascends the AGB. The separation of the absorption (class 30) and emission (class 20) objects in the color-color diagram suggests that the color of AGB stars also changes as star evolves. Most interestingly, the class 20 and 30 sources lie on a band in the color-color diagram which can be interpreted as an evolutionary sequence (Olnon *et al.* 1984; Kwok, Hrivnak, and Boreiko 1987). Since the photospheres of late AGB stars are not directly observable and their distances are unknown, the existence of this empirical sequence makes the color-color diagram more useful than the H-R diagram for the purpose of testing of theoretical AGB evolutionary models. In this section, we will develop the basic model for the evolution on the AGB and compare the model results with the *IRAS* data.

a) Evolution of an AGB Star

The calculation of a stellar evolutionary track with mass loss is a complicated task. Fortunately, the cores of AGB stars are essentially decoupled from their envelopes. Mass loss from the surface removes mass from the envelope but does not interfere with the nuclear processes near the core. Static models of AGB stars show that the stellar luminosity is mainly a function of the core mass, and this dependence is expressed in the well-known core mass-luminosity relationship first proposed by Paczyński (1971):

$$\begin{aligned} L_* &= L_0(M_c - M_0) \\ &= 59250(M_c - 0.495) \end{aligned} \quad (2)$$

(Iben and Renzini 1983), where L_* and M_c are respectively the luminosity and core mass of the star in solar units. Since mass of the core increases as the nuclear burning proceeds, we have

$$\frac{dM_c}{dt} = \frac{L_*}{xE_H}, \quad (3)$$

where $x(=0.7)$ is the hydrogen mass abundance and $E_H = 6 \times 10^{18}$ ergs is the energy released by converting 1 g of hydrogen into helium. Substituting equation (2) into equation (3), we have

$$\dot{M}_c = 8 \times 10^{-7}(M_c - 0.495)\, M_\odot \text{ yr}^{-1} . \quad (4)$$

Integrating equation (4) gives

$$M_c(t) - M_c(0) = [M_c(0) - 0.495][\exp(t/t_0) - 1] , \quad (5)$$

where $t_0 = 1.2 \times 10^6$ yr and $M_c(0)$ is the initial core mass at the beginning of AGB. In our models, the values of $M_c(0)$ used are those given by Iben (1981). We can see from equations (2) and (5) that stellar luminosity on the AGB increases exponentially with time.

The evolution of the envelope with time is more uncertain for it is dependent on the rate of mass loss. Assuming that the mass-loss formula $\dot{M}(t) = f(L_*, M_*, R_*, \ldots)$ is known, then the envelope mass $M_{en}(t)$ is given by

$$M_{en}(t) = M_{en}(0) - \int \dot{M}(t)dt . \quad (6)$$

For certain forms of $\dot{M}$, the above equation can be integrated and the total mass of the star ($M_* = M_c + M_{en}$) can be expressed in a closed form (see Appendix). In other cases, M_* can be obtained numerically.

After the solutions of $M_*(t)$ and $L_*(t)$ are obtained, the effective temperature of the star can be approximated by

$$\log_{10}(T_*) = [101.49 - 2.5 \log_{10}(L_*) + 0.533\, M_*]/26.64 \quad (7)$$

(Wood and Cahn 1977). The radius of the star (R_*) can then be obtained by

$$R_*(t) = \{L_*(t)/[4\pi\sigma_* T^4(t)]\}^{1/2} , \quad (8)$$

where σ is the Stefan-Boltzmann constant. In the late stages of AGB evolution, the star is likely to be pulsating in the fundamental mode and the pulsation period (P) can be written as

$$\log_{10} P = -1.96 - 0.67 \log_{10} M_* + 1.87 \log_{10} R_* \quad (9)$$

(Ostlie, Cox, and Cahn 1982).

b) The Circumstellar Envelope

Since L_* grows exponentially (eqs. [2] and [5]), all stellar parameters are expected to be evolving rapidly during the late AGB. The mass-loss rate is also changing on a short-time scale, and the traditional assumption of constant mass loss is likely to break down. This will cause a steep density gradient in the circumstellar envelope which should have observational consequences.

If we assume that the stellar wind velocity (V) is not changing with time, then the density profile $\rho(r, t)$ of the circumstellar envelope can be derived from the equation of continuity:

$$\dot{M}(t - r/V) = 4\pi r^2 V \rho(r, t) . \quad (10)$$

We can normalize the density profile with respect to the dust condensation radius (r_0) by introducing the function $\xi(r, t)$ defined by

$$\rho(r, t) = \rho(r_0, t)\, \xi(r, t) . \quad (11)$$

Assuming that the dust and gas are uniformly mixed, then the dust mass-loss rate ($\dot{M}_d$) can be written as

$$\dot{M}_d = \frac{Ayf}{\mu} \dot{M} = \psi \dot{M} , \quad (12)$$

where μ is the mean atomic weight of the gas per hydrogen atom, A is the molecular weight of the grain material, y is the cosmic abundance of the least abundant element in the grain, and f is the fraction of that element condensed in solid form.

The optical depth of the circumstellar envelope at wavelength λ_0 is then given by

$$\tau(\lambda_0) = \int_{r_0}^{\infty} \pi a^2 Q(\lambda_0) N_d(r) dr , \quad (13)$$

where $N_d(=\psi\rho/m_d$, m_d = mass of each grain) is the grain number density in the envelope, $\pi a^2 Q$ is the grain absorption cross section. There are reasons to believe that the grain size distribution in the circumstellar envelope is determined by grain-gas sputtering (Kwok 1975; Biermann and Harwit 1980) and in the absence of further information, we will assume a uniform grain size for the entire envelope. In such a case, the optical depth at any time t can be written as

$$\tau(\lambda_0) = \pi a^2 Q(\lambda_0) N_d(r_0) \int_{r_0}^{\infty} \xi(r, t) dr . \quad (14)$$

Combining equations (10)–(14), we have

$$\dot{M}(t - r_0/V) = C(F/r_0)^{-1} \tau(\lambda_0) r_0 V , \quad (15)$$

where $C = (16\pi/3)(\rho_d/\psi)(a/Q)$, ρ_d is the density of the grain

material, and $F(t)$ is the integral of $\xi(r, t)$ over $r > r_0$. This implies that

$$\frac{F}{r_0} = \frac{1}{r_0}\int_{r_0}^{\infty} \frac{\rho(r)}{\rho(r_0)}\, dr \qquad (16)$$

is a pure number which is equal to unity for an inverse square density profile. The constant C in equation (15) is a function of the grain parameters only. Once the mass-loss formula is specified, then equation (15) implies that the entire structure of the circumstellar envelope is determined by the condensation radius r_0 and the optical depth.

We will assume that the dust grains will condense as soon as the dust equilibrium temperature drops below 1500 K. This suggests that r_0 will change as the star evolves and has values of between 7 and $4R_*$ from the beginning to the end of the AGB. As a result, τ is the only remaining free parameter and will be chosen to best reproduce the emission or absorption strength of the 10 μm silicate feature.

IV. THE RADIATIVE TRANSFER MODEL

a) *The Numerical Procedure*

The radiative transfer program which was used to produce the model spectra was adapted from the program DUSTCD developed by C. M. Leung for the modeling of the dust in molecular clouds and star-formation regions. The program and the method of solution of the equations of radiative transfer are fully described in Leung (1975, 1976) and Spagna and Leung (1983). The DUSTCD code has been modified to apply to a stellar wind situation. A spherically sysmmetric circumstellar dust envelope of a certain dust density profile is assumed to be heated by a central star. The equation of transfer is solved in an iterative manner to yield the source function at each part of the envelope. The intensity distribution and the total emergent flux are then calculated from the derived source functions.

In the program the method of finite difference is used to carry out the numerical integration of the basic equations given in Leung (1975). For each frequency under consideration the cloud is divided into a number of radial shells which are defined by a radial grid. In the present calculations, a radial grid of 121 points and a frequency grid of 120 wavelengths were used. The computer code was run on the University of Calgary CYBER 205 Supercomputer and convergence is achieved after a few minutes of computer time for most models.

Since most of the optical depth is concentrated in the inner regions of the dust shell and the density gradient in the envelope often leads to a steep temperature gradient, the radial grid was arranged logarithmically out from the dust condensation radius to an outer radius 1000 times this radius. There are 40 grid points per factor of 10 change in radius instead of the approximately linear grid which was used for modeling of molecular clouds by Leung.

In running the program the stellar properties were set and then a number of trials were done to set the inner radius to the appropriate value for a dust condensation temperature of 1500 K. A reasonable estimate of the inner radius could be found by assuming the dust to act as a thin opaque shell. From the results of a first run with this inner radius the value could be adjusted to produce the desired maximum temperature after a few trials.

Once the output spectrum was obtained it was converted to effective *IRAS* colors by numerically integrating over the filter profiles given in the *IRAS Explanatory Supplement* (1985). These values were then directly compared with the *IRAS* photometric data. The model spectra were also normalized for comparison with the LRSC data. One can estimate the distance to specific objects by comparison of the model fluxes with the *IRAS* fluxes, which turns out to yield distances of 1 to 2 kpc for typical emission feature objects. This is consistent with the galactic distribution of these sources. It thus shows that the luminosities of the objects are consistent with what is expected for AGB stars.

b) *The Dust Parameters*

The chemical composition of the dust is assumed to be $(Mg, Fe)_2\ SiO_4$ (Gilman 1969), with a corresponding molecular weight (A) of ~ 140 amu. Since the grain condensation is likely to be limited by the abundance of silicon, we have $y \sim 4 \times 10^{-5}$. Assuming complete condensation ($f = 1$) and $\mu = 1.3$, we have a dust-to-gas ratio of $\psi = 4.3 \times 10^{-3}$. With $\rho_d \sim 3$ g cm^{-3}, equation (13) shows that the only free parameter left in the model calculation is Q/a. In the present calculation, we assume the value of Q/a at 9.7 μm to be 5.25 μm^{-1}. The constant C in equation (15) can therefore be evaluated and yields a value of $1.090 \times 10^{-3}\ M_\odot\ \mathrm{yr}^{-1}\ \mathrm{pc}^{-1}\ (\mathrm{km\ s}^{-1})^{-1}$.

c) *The Dust Opacity Function*

Since the LRS spectra represent some of the best quality spectra of AGB stars in the wavelength region of 8–23 μm, we have the opportunity of obtaining a better dust opacity function than previously available. In the case of low optical depths in the envelope, one expects that the emergent spectrum will directly reflect the shape of the opacity function. Models were compared with objects in our working sample which have closely matching colors, particularly on the 12/25/60 μm color-color diagram where the color evolution is clearly related to the feature strength. In particular, major improvements in the opacity function have been made around the 12–20 μm region which has not been well determined in previous ground-based observations.

Since very little is known about the 18 μm feature, we have run models with a ratio of the 18 to 10 μm feature ranging from 0.4 to 0.7. A final value of 0.5 is chosen for the following calculations. There are indications from the LRS data that the 18 μm feature strength may not be constant for all the sources and the value of 0.5 should be viewed as an average value.

We also attempted to deduce the long-wavelength opacity function from the *IRAS* photometric colors. As the result of a few trails, the opacity function was set to have a λ^{-1} functional form out to 84 μm and a λ^{-2} functional form thereafter. The final form of the dust opacity function which was obtained from the models is presented in Figure 8, normalized to the 9.7 μm peak value. It provides a reasonable fit to the LRSC data for spectra over the entire range from strong emission features to strong absorption features.

V. MODEL RESULTS

Our objective is to find a mass-loss formula which will satisfy the evolutionary requirements as described in § III*a* and at the same time being able to recreate the color and dust-feature evolution in AGB stars. In this section, we will discuss primarily the results from one mass-loss formula and another example will be described in the Appendix.

One of the most widely used mass-loss parameterizations for the late-type giant stars is the Reimers formula

$$\dot{M} = 4 \times 10^{-13} \eta L_* R_* M_*^{-1}\ M_\odot\ \mathrm{yr}^{-1}\ , \qquad (17)$$

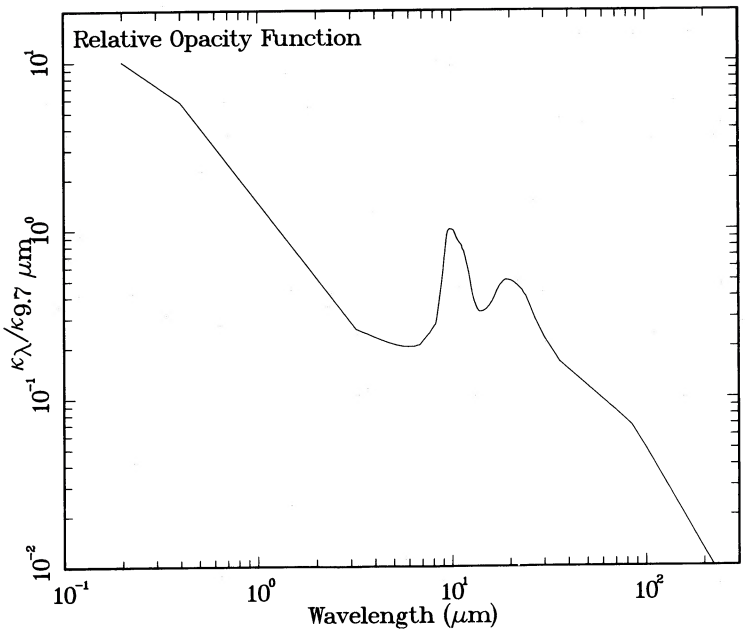

FIG. 8.—The dust opacity function

where η is an arbitrary factor usually assumed to be tween 3 and 0.33 (Reimers 1977). The underlying physical principle of this formula is that a constant fraction of the stellar luminosity is expended on the stellar wind with the stellar wind velocity being proportional to the stellar escape velocity. This formula was derived for K-type and early M-type stars and cannot be directly applied to AGB stars. With a coefficient of $\eta = 1$, the amount of mass loss is inadequate and at the end of the AGB phase there is still a large amount of mass in the envelope for stars of initial mass near 8 $M_\odot$. A process called the "superwind" is frequently invoked to remove the remaining material over a short time period in order to satisfy the requirement that such a star becomes a white dwarf star and planetary nebula at the end of its life. Not only is this proposal ad hoc, it is also inconsistent with the high mass-loss rates observed in AGB stars determined by infrared (Gehrz and Woolf 1971) and radio techniques (Knapp *et al.* 1982). It would be more desirable to assume one mass-loss formula which has a continuous range of mass-loss rates and is consistent with observed rates of mass loss from AGB stars.

The fact that the observed silicate feature ranges from strong emission to strong absorption suggests that there must be a large range of mass-loss rates for stars on the AGB. If one assumes that an 8 $M_\odot$ star is the maximum white dwarf progenitor (Weidemann and Koester 1983), then a value of $\eta = 4.5$ is required to keep a star from becoming a supernova. However, the $\dot{M}$ values for a lower mass star predicted by this constant are higher than those which are observed. In order to satisfy both ends of the mass range the simplest alternative is to assume that η is a function of the initial stellar mass. A linear relationship serves quite well, producing $\dot{M}$ values near 10^{-7} $M_\odot$ yr^{-1} for a 1 to 1.5 $M_\odot$ star at the start of AGB evolution and values of near 10^{-4} $M_\odot$ yr^{-1} for the more massive stars near the end of the evolution. The observed range of $\dot{M}$ values can therefore be produced by one mass-loss formula of the following form:

$$\dot{M} = 1.8 \times 10^{-12}[M_*(0)/8\ M_\odot]L_* R_* M_*^{-1}\ M_\odot\ \mathrm{yr}^{-1}\ , \quad (18)$$

where $M_*(0)$ is the main-sequence mass of the star.

The characteristics of the mass-loss evolution for this formula are illustrated in Figure 9 where the $\dot{M}$ evolution for stars of initial mass 1.5 and 8 $M_\odot$ are shown in the mass-luminosity diagram. The horizontal axis can also be considered as a linear time axis and the time scale is shown in the upper horizontal axis. The AGB evolution lasts 1.2×10^6 yr. for the 1.5 $M_\odot$ model and 5.2×10^5 yr for the 8 $M_\odot$. We can see that the 8 $M_\odot$ model shows a dramatic increase in $\dot{M}$ over the last few 10^4 yr of the evolution. The dotted lines are curves of constant periods calculated by equation (9) and most of the stars with long (>1000 days) pulsation periods are stars of high (>2 $M_\odot$) progenitor masses.

The spectral evolution of a star with an initial mass of 1.5 $M_\odot$ is illustrated in Figures 10*a* to 10*d*. The mass-loss rate ranges from 2×10^{-7} $M_\odot$ yr^{-1} at the beginning of the AGB to 1.8×10^{-6} $M_\odot$ yr^{-1} when the core is exposed. The highest optical depth at 9.7 μm achieved in this model is $\sim$4, and during most of the evolutionary lifetime, the silicate feature is in emission. Under each of the model spectra, an observed spectrum for a source chosen from the working sample is also displayed for comparison. We can see that the observed LRS spectra for AGB stars are successfully approximated by the model results.

The corresponding spectral evolution for an 8 $M_\odot$ star is shown in Figures 11*a* to 11*d*. In this case, the total evolutionary lifetime of the AGB is only 5.22×10^5 yr. The range for mass-loss rates is 6.7×10^{-6} to 9×10^{-5} $M_\odot$ yr^{-1}, and the corresponding optical depths at 9.7 μm are between 6.7 and 49. During the entire AGB phase, this 8 $M_\odot$ star has the silicate feature in absorption.

It is interesting to note that the transition of the silicate feature from emission to absorption occurs at $\tau \sim 4$, in approximate agreement with the inverse-square density model of Jones and Merrill (1976). This is because the absorption feature is created by absorbing against the continuum emitted by warmer dust near the star but not against the photosphere. The envelope optical depth at 10 μm is therefore much greater than the strength of the silicate feature defined by

$$s = -\ln\,(F_{9.7\mu m}/F_{\mathrm{cont}})\ , \quad (19)$$

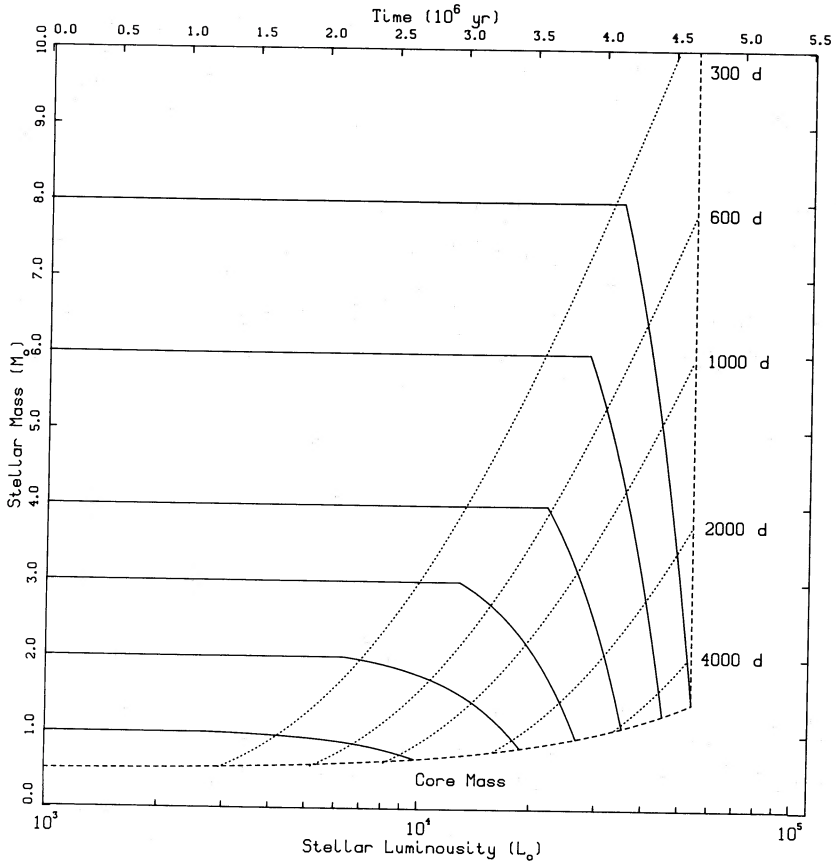

FIG. 9.—The mass-luminosity diagram for AGB evolution under the mass-loss formula in eq. (18). The dotted lines are curves of constant pulsation periods as given in eq. (9).

which is often referred to (erroneously) in the literature as a measure of the optical depth.

For most of the models the 18 μm feature does not appear very strong compared to the 10 μm feature. This is particularly true for optical depths from ~ 3 to 20 at 10 μm, where one almost does not see the 18 μm feature in the model spectra. The weakness of the 18 μm feature can be understood that in this range of optical depths, the 18 μm feature is in transition from emission to absorption. Since it requires a larger amount of cool dust for the 18 μm to go into self-absorption, it is not surprising that the 18 μm absorption feature appears much later than the 10 μm feature. Assuming a ratio of peak opacity (κ) of 0.5 (see § IV*c*), our models suggest that the 18 μm feature does not go into absorption until $\tau(10\ \mu\text{m})$ is greater than ~ 40.

The model spectra are also convolved with the instrumental profiles of the *IRAS* filters to produce simulated photometric measurements at 12, 25, 60, and 100 μm. The results at different epochs are plotted in the color-color diagrams in Figures 12 and 13 together with the distribution of the class 20 and 30 sources in the working sample. The evolutionary tracks for two stellar masses (1.5 and 8 $M_\odot$) are shown. Each triangle on the tracks represent an interval of 10^5 (4×10^4 near the end of 8 $M_\odot$ case) years in time. The last five points on each track represent evolution beyond the end of the AGB, after mass loss has terminated. The behavior of post-AGB evolution will be discussed in a subsequent paper (Volk and Kwok 1988). While the 1.5 and 8 $M_\odot$ tracks have only limited overlapping areas on the color-color diagram, evolutionary tracks for intermediate masses have varying degree of overlap with these two curves depending on the initial mass.

None of the tracks we calculated goes up to the area occupied by the class 70 sources. As discussed in § II*b*, we believe that most of the class 70 sources are H II regions or infrared sources embedded in interstellar clouds and are not relevant to evolution on the AGB.

In Figures 9 and 10 the 18 μm feature generally seems to be weaker than the LRS data would indicate. Bedijn (1987) finds that a stronger 18 μm feature produces a greater upward curvature on the 12/25/60 μm color-color diagram. If this is true, then a stronger 18 μm feature would produce better agreement with the data in Figure 12. However, there are a number of class 20 LRS spectra that are very smooth from 13 to 20 μm but have strong 10 μm features. It is not clear why these sources should lack the 18 μm emission feature. One possibility is that the grain composition (and therefore the opacity function) change as the star evolves.

The evolution of the dust optical depth with time for AGB stars of initial mass values of 1.5, 3, 6, and 8 $M_\odot$ is shown in Figure 14. The horizontal line at $\tau \sim 4$ indicates where the 10 μm feature passes from emission to absorption. The present mass-loss formula therefore implies that infrared sources with the silicate feature in absorption are primarily stars with high ($>3\ M_\odot$) progenitor masses. We should not that this transition optical depth of ~ 4 is independent on the dust condensation temperature chosen. If the dust condenses further out as the result of a lower assumed condensation temperature, then

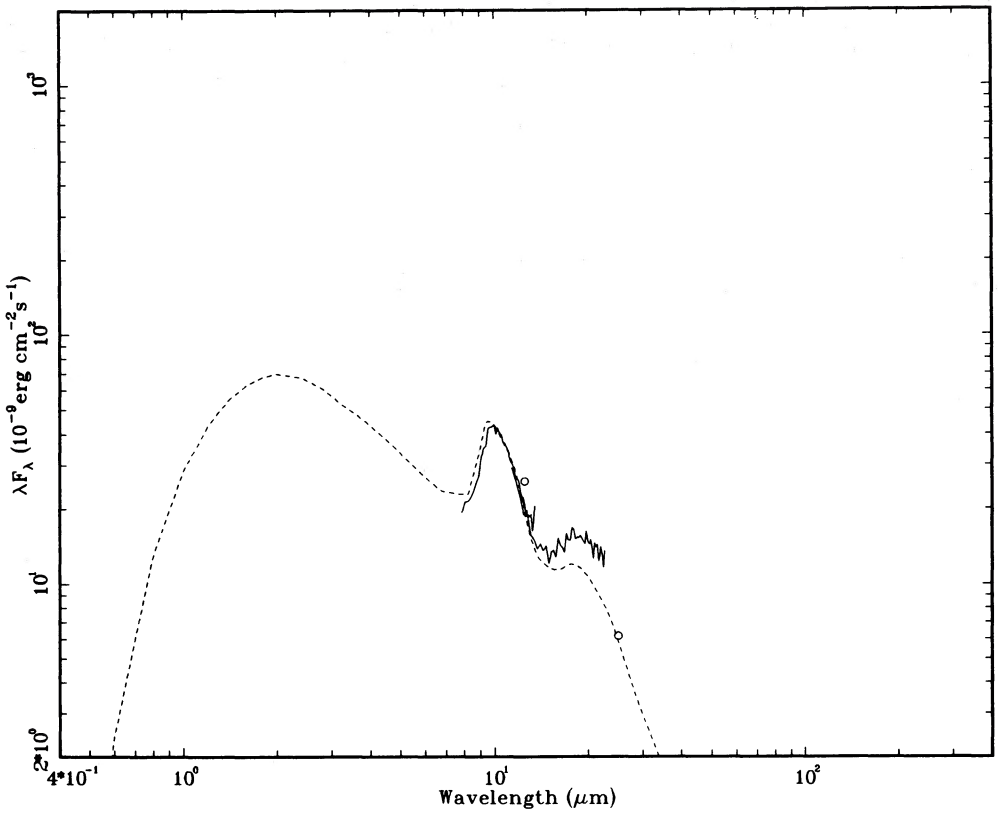

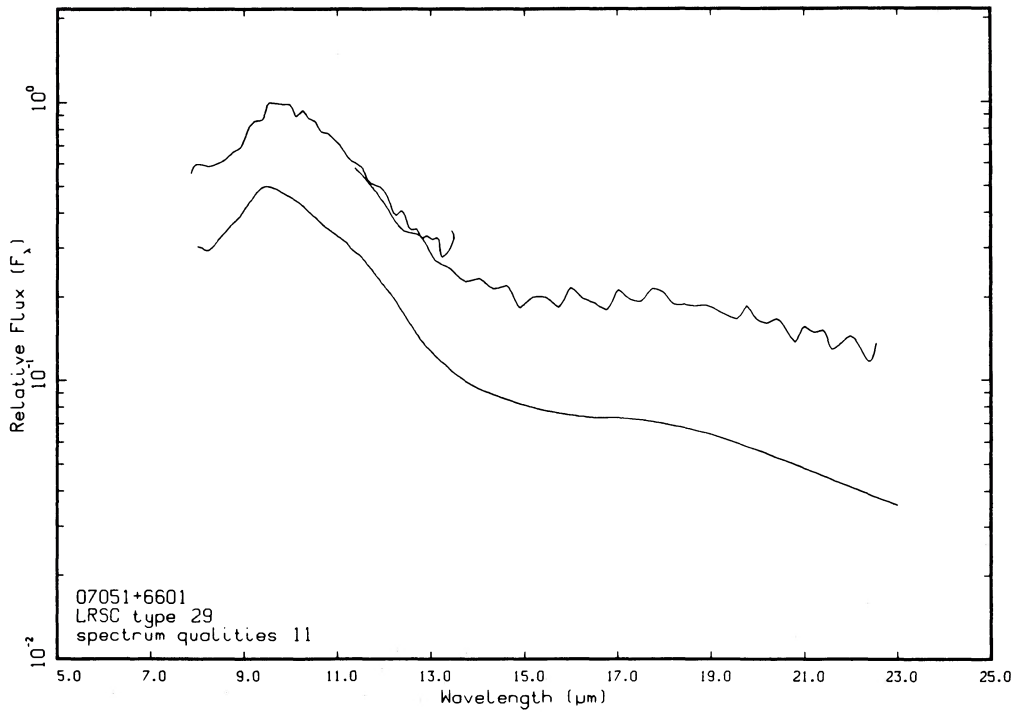

FIG. 10*a*

FIG. 10*a*–10*d*.—Evolution of the spectrum of a 1.5 $M_\odot$ star from the beginning to the end of the AGB. The lower half of each figure shows the comparison of the model spectrum with an observed spectrum of a source chosen from the working sample.

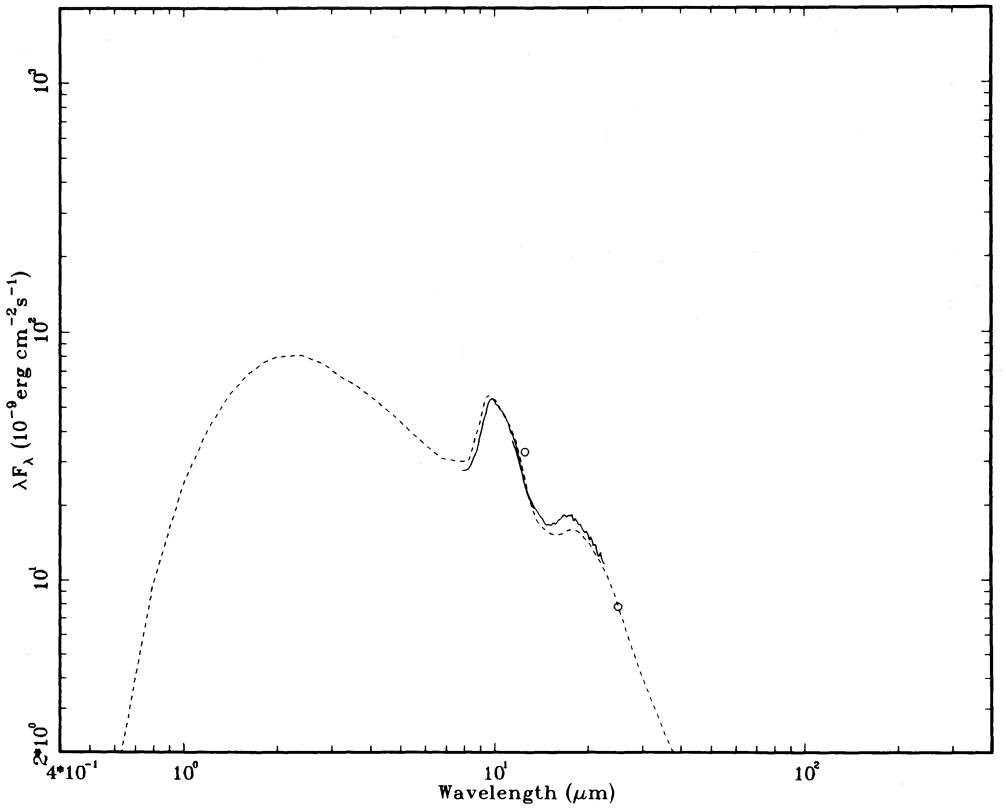

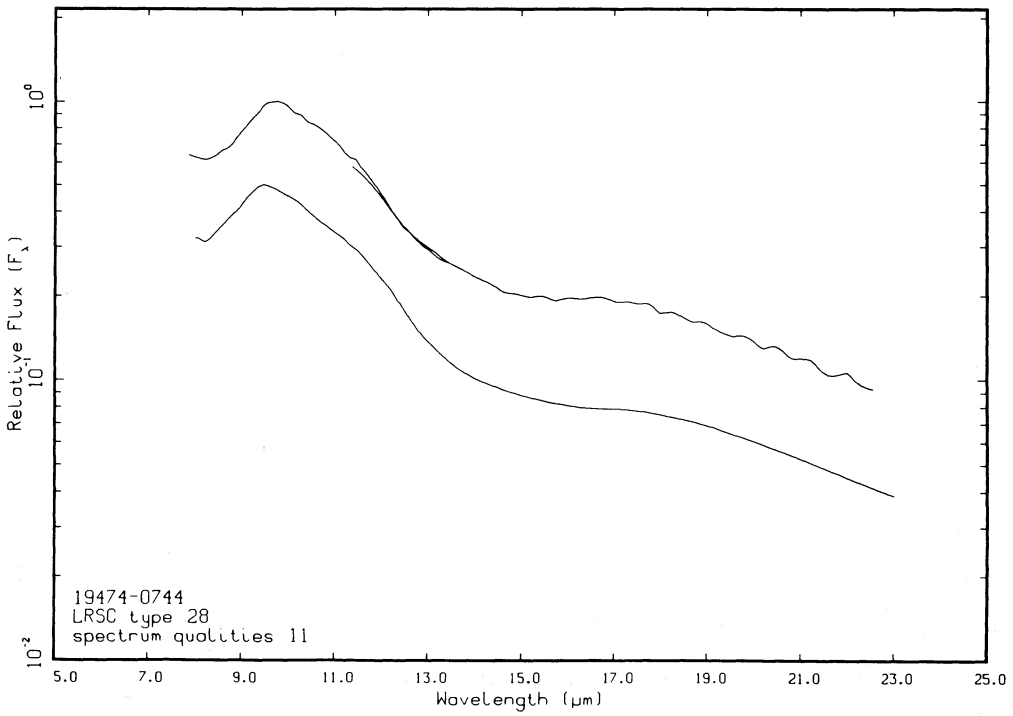

FIG. 10*b*

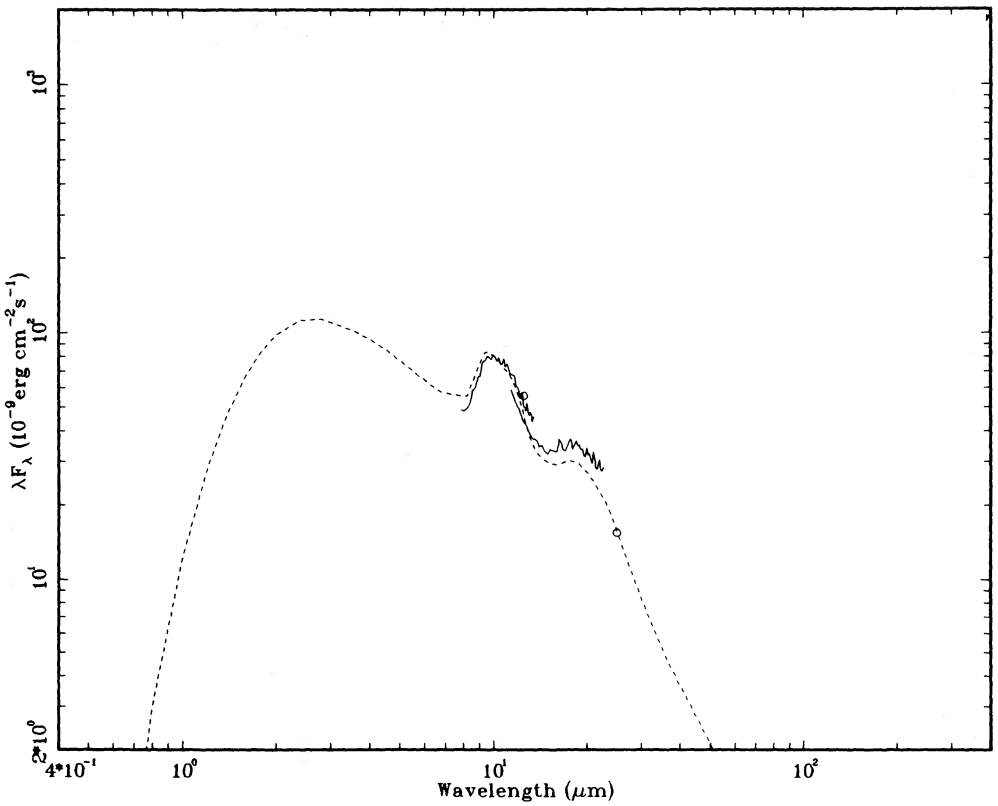

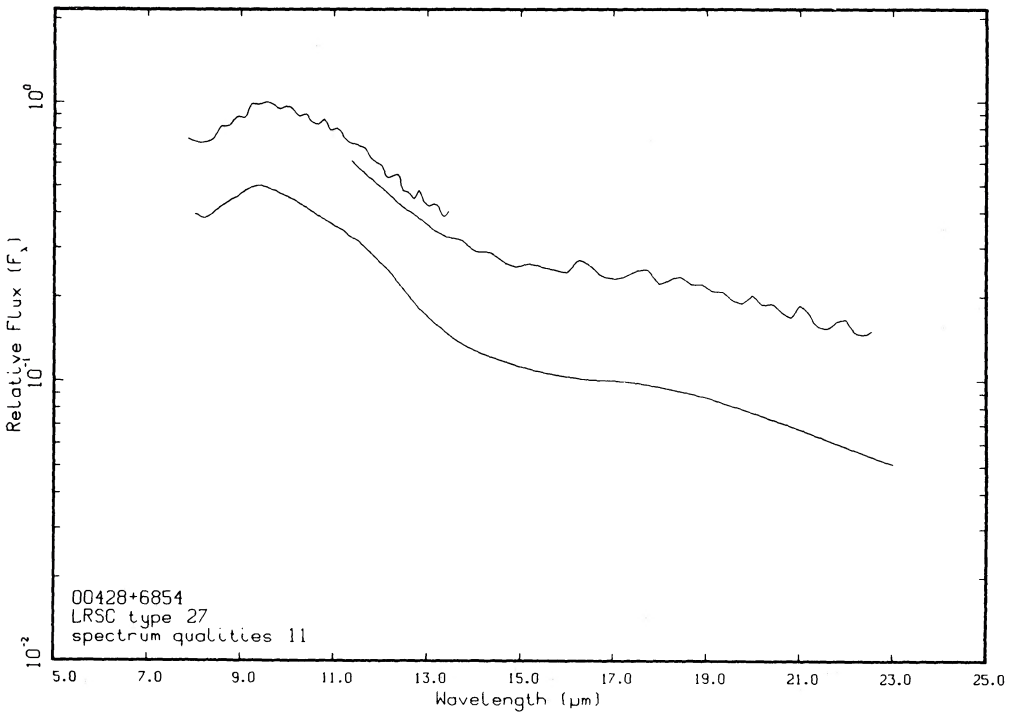

FIG. 10*c*

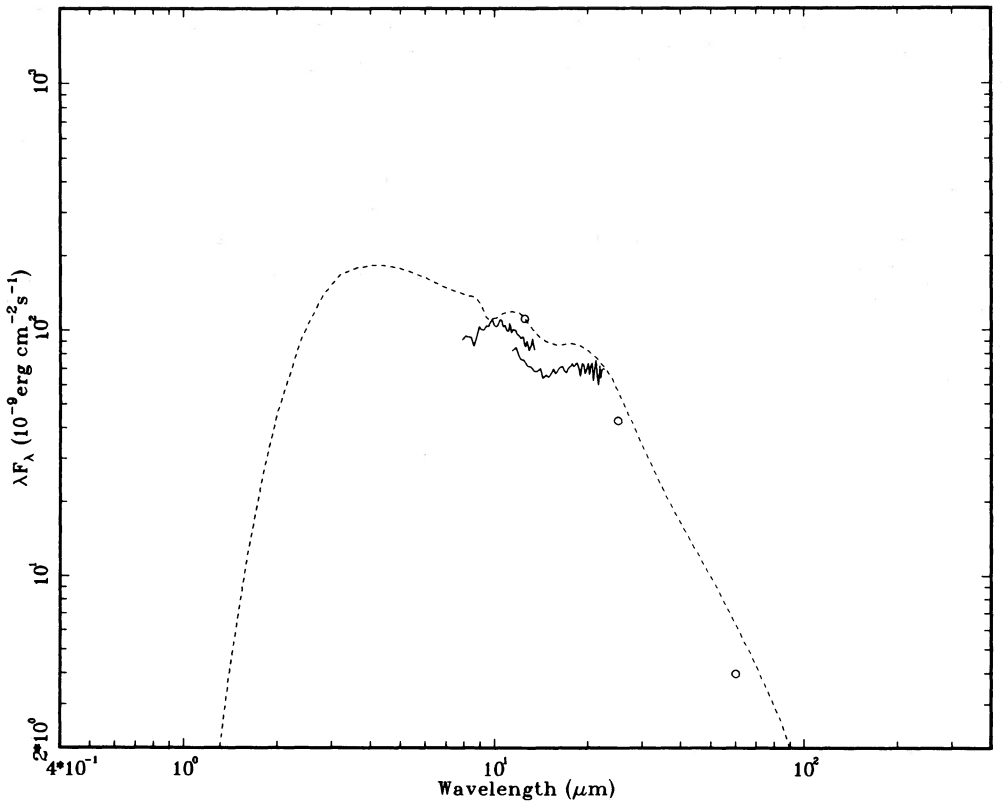

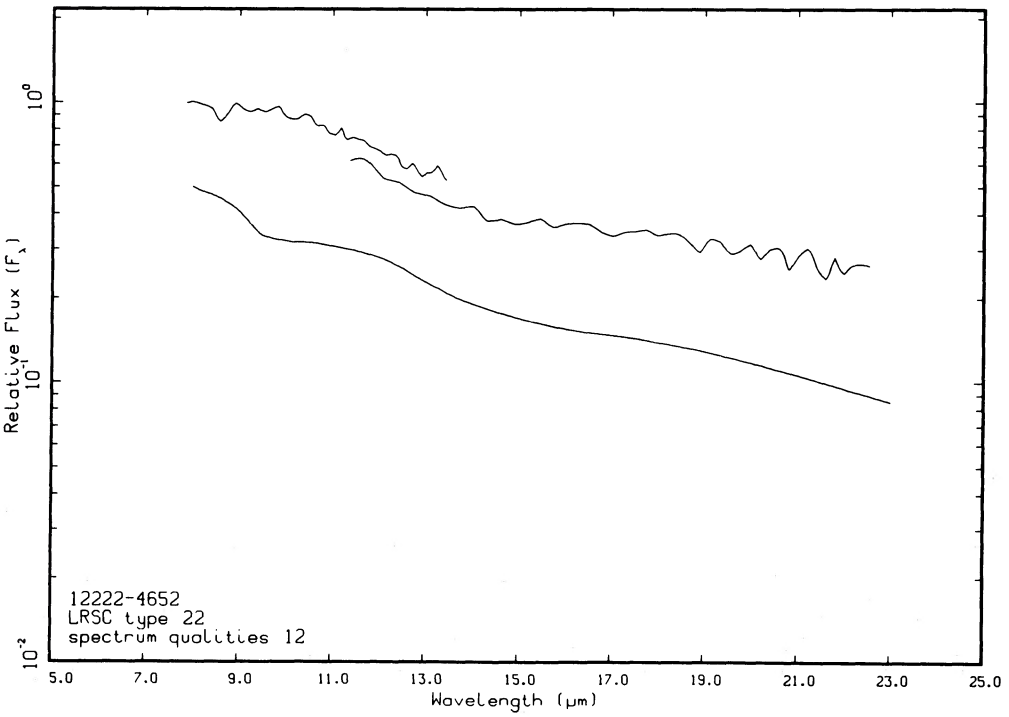

FIG. 10*d*

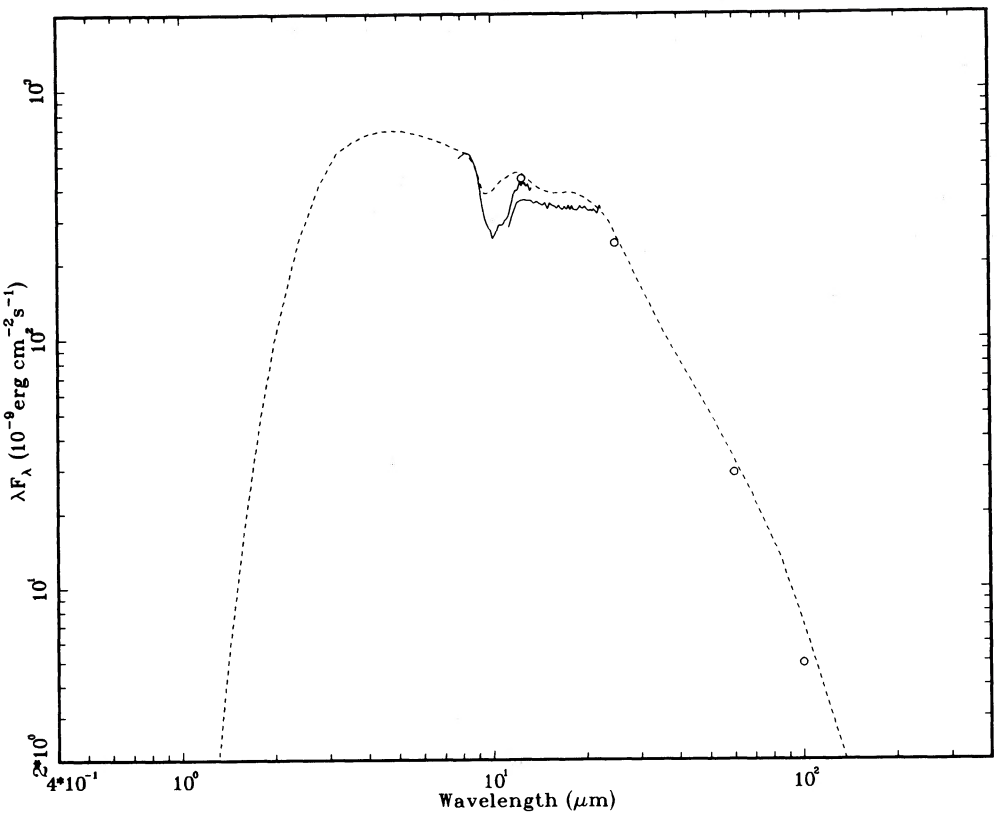

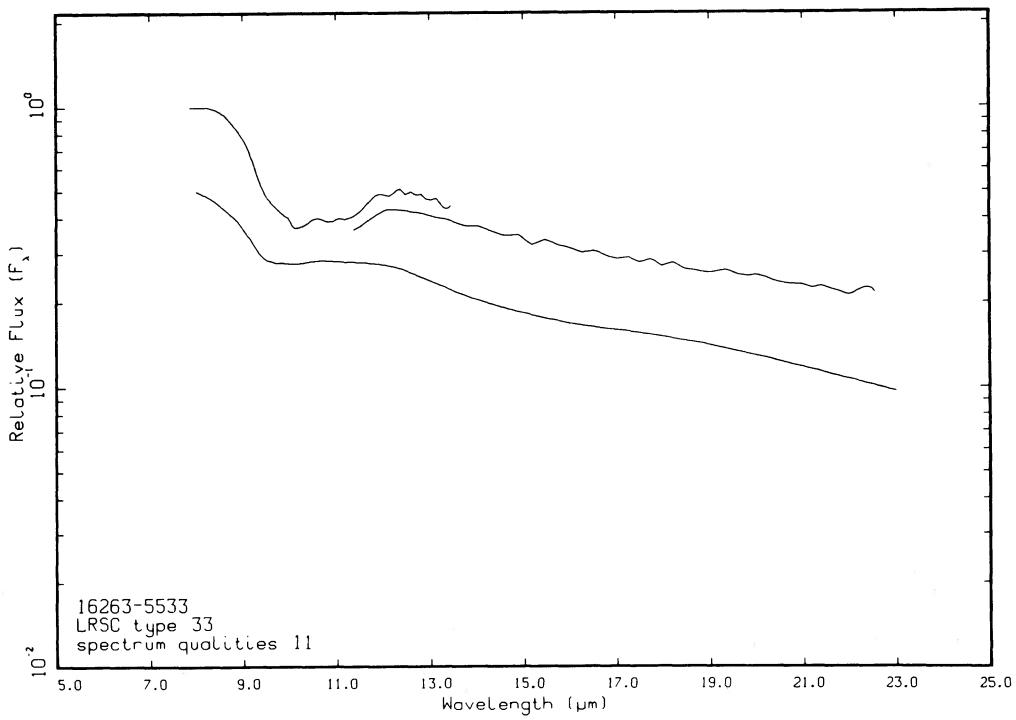

FIG. 11*a*

FIG. 11*a*–11*d*.—Evolution of the spectrum of an 8 $M_\odot$ star

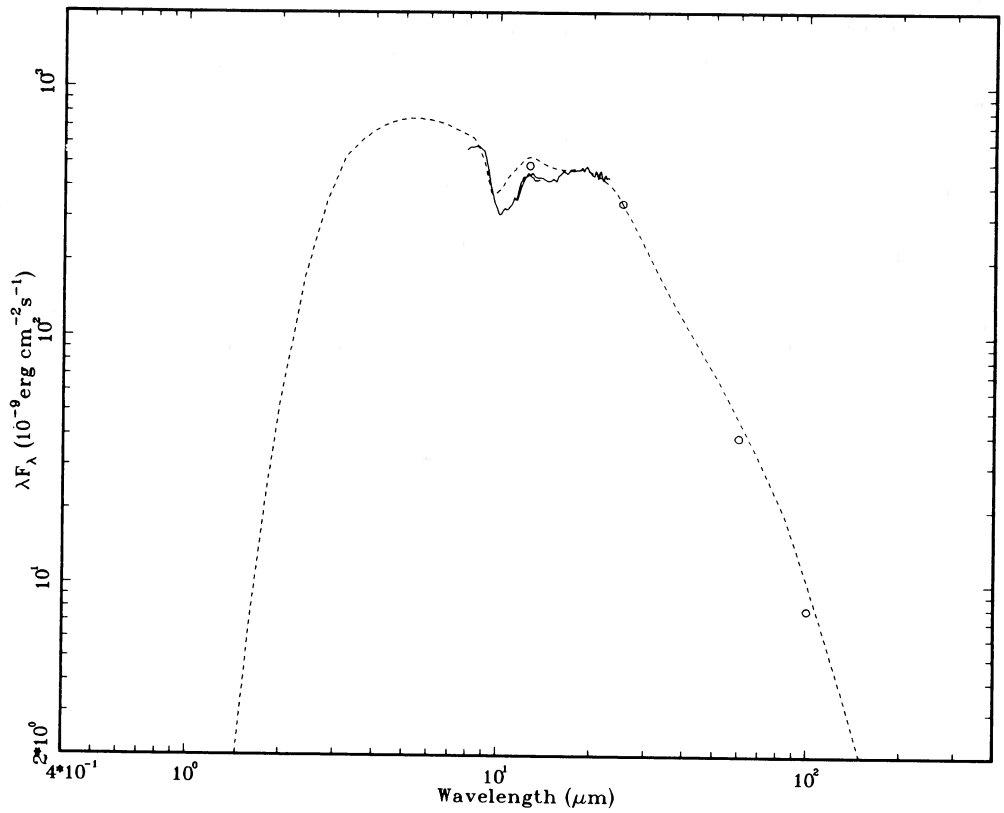

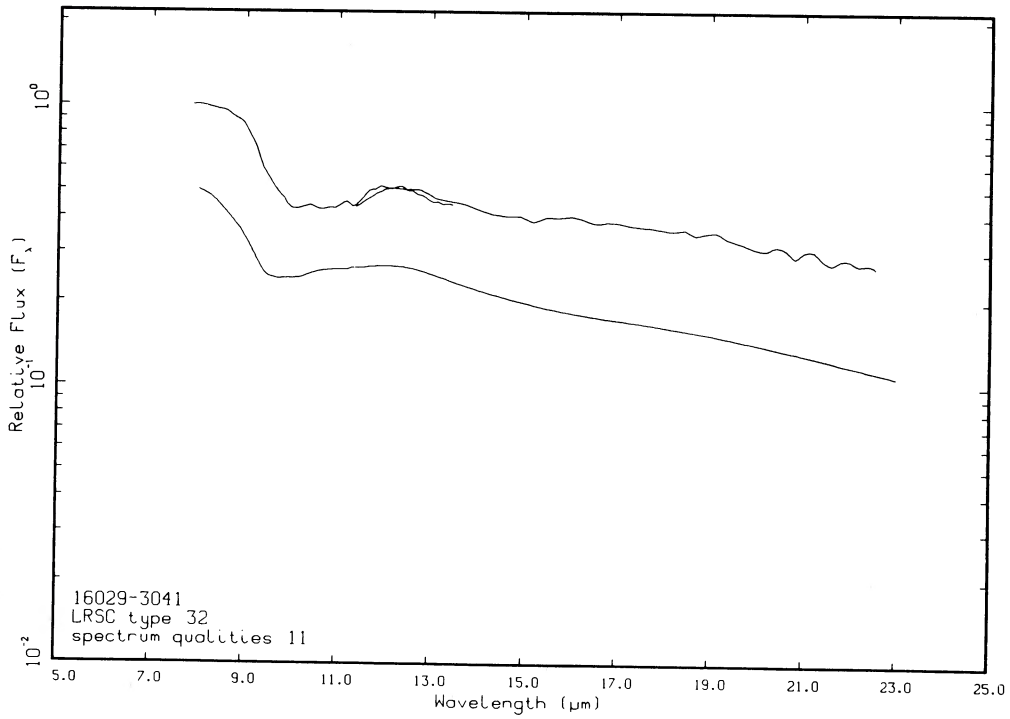

FIG. 11*b*

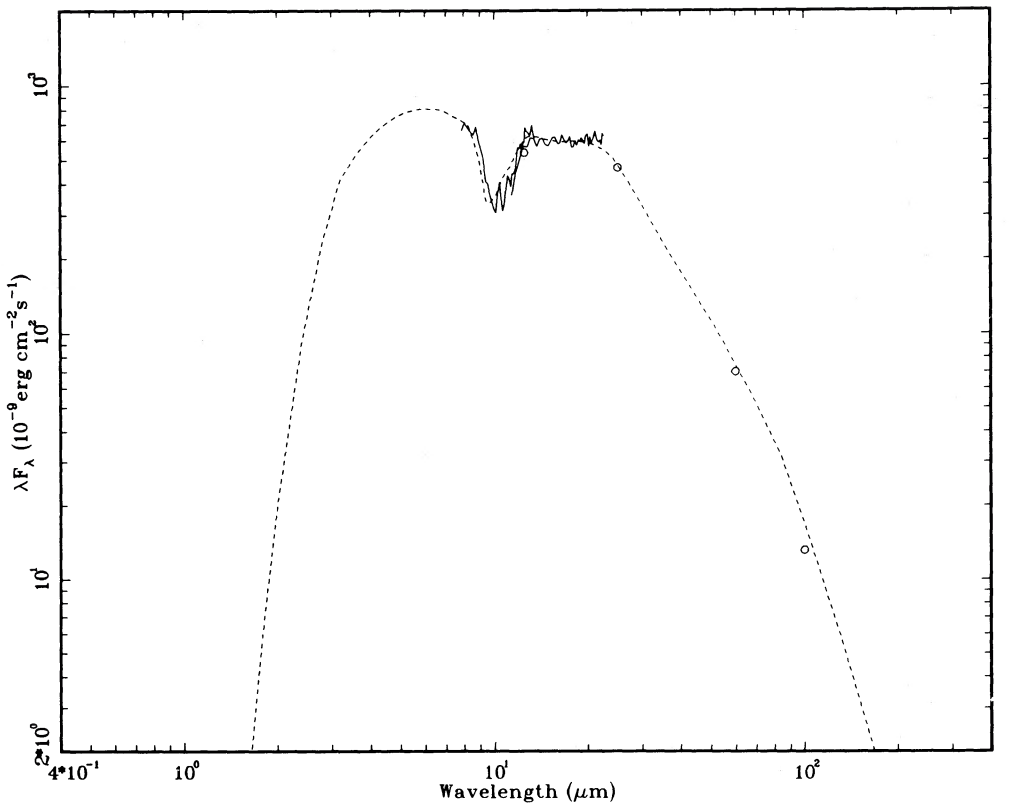

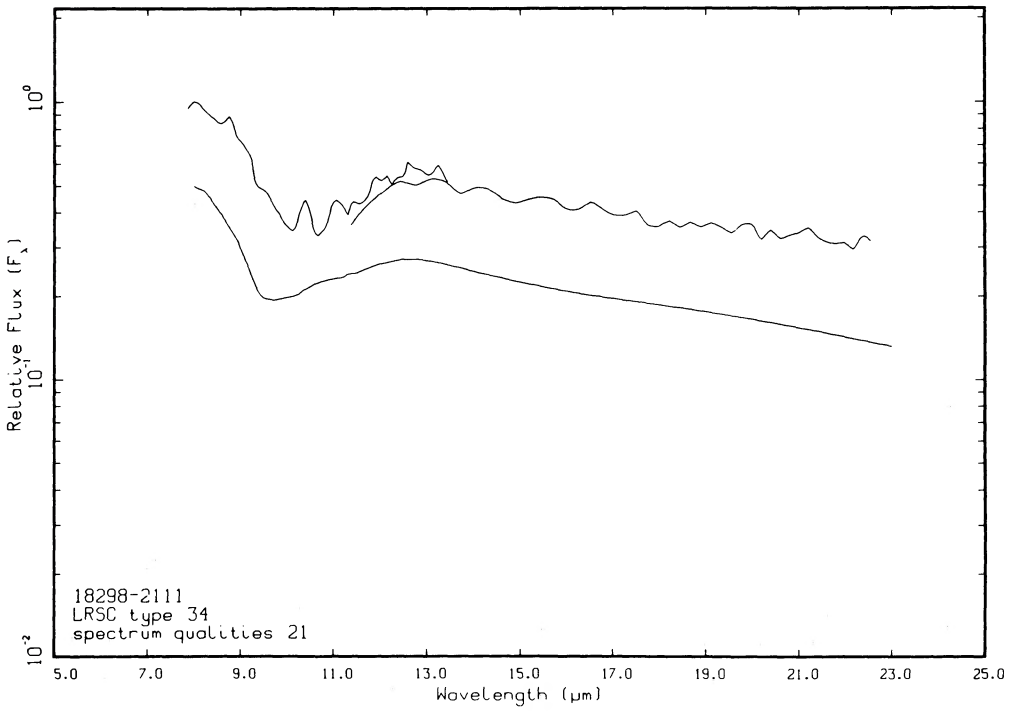

FIG. 11*c*

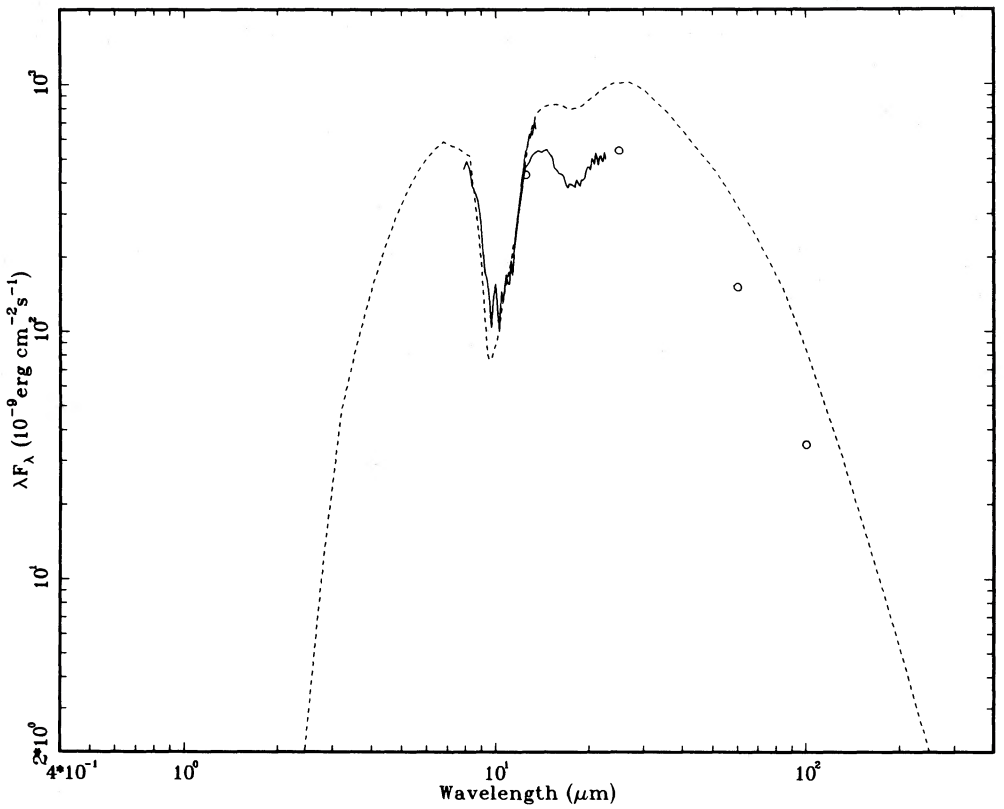

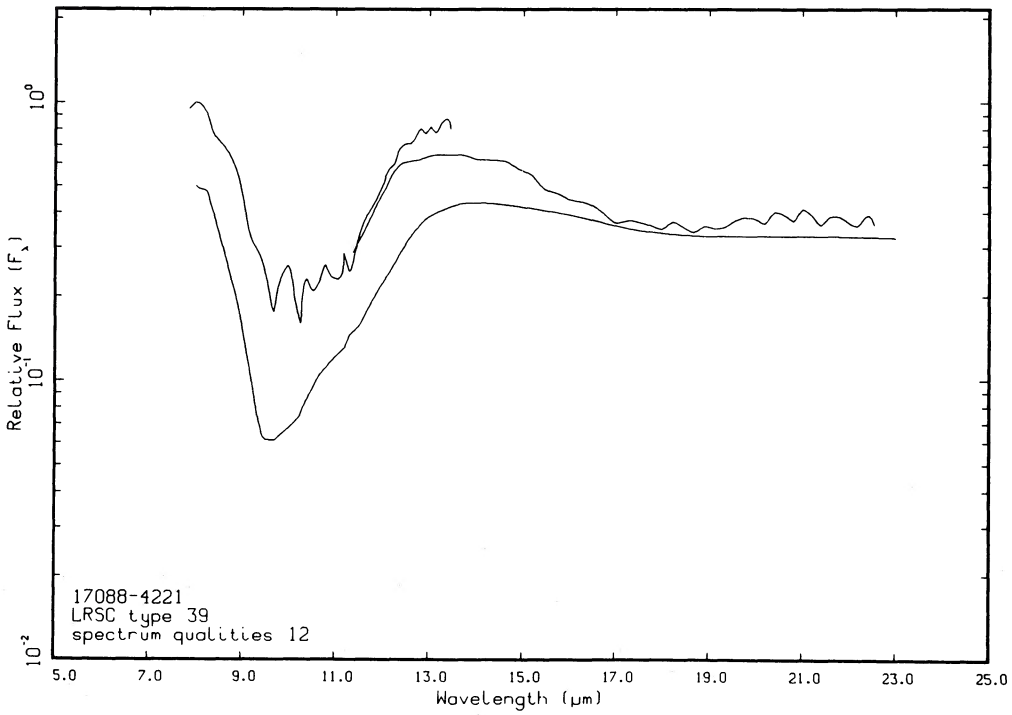

FIG. 11*d*

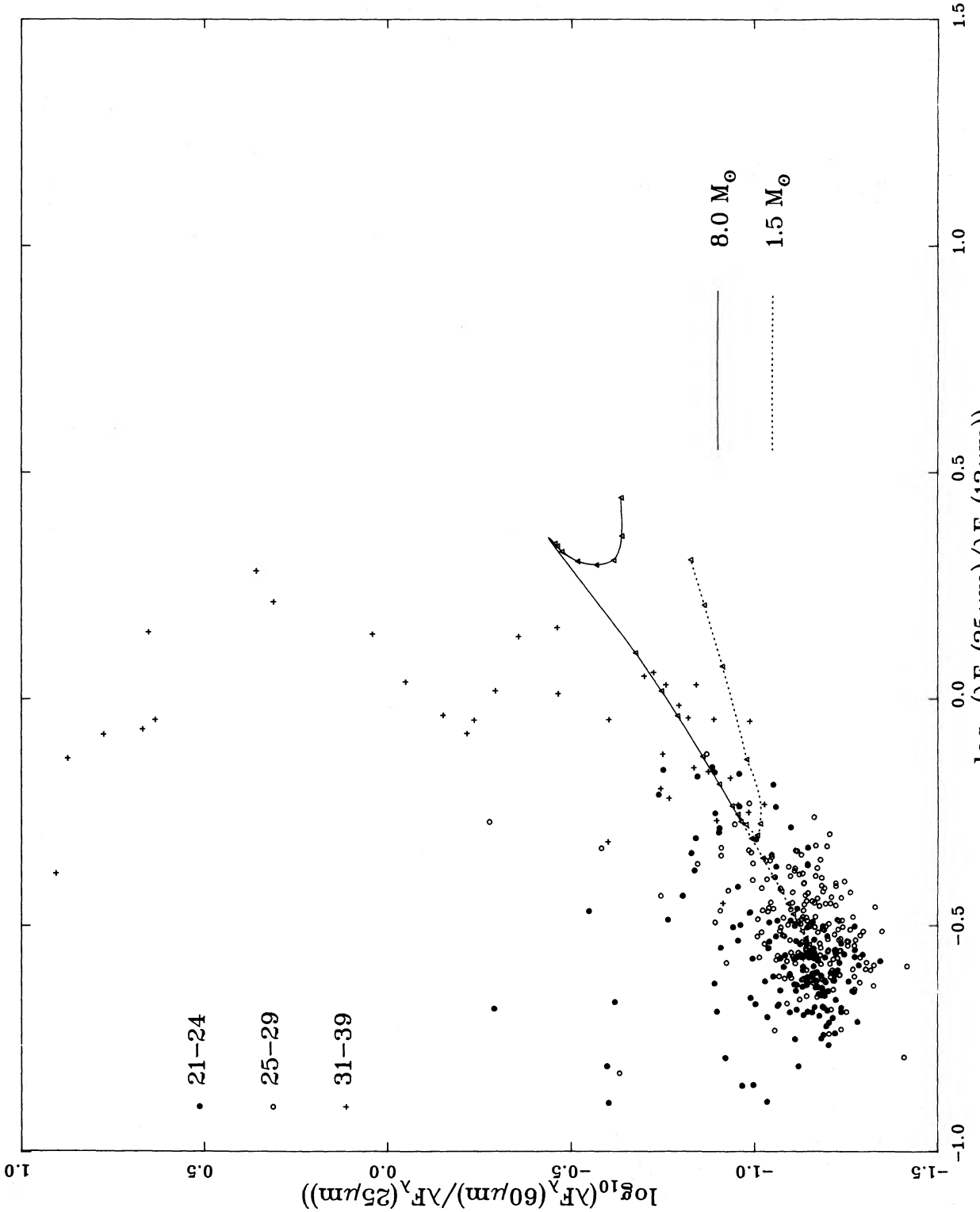

FIG. 12.—The evolutionary tracks on the 12/25/60 μm color-color diagram for AGB stars with initial masses 1.5 and 8 $M_\odot$. The time steps (10^5 yr) are indicated by triangles on the curves. The last five points on each track represent evolution beyond the AGB. Also plotted are sources in the working sample. Note that most of the sources with $\log_{10}[\lambda F_\lambda(60\ \mu m)/\lambda F_\lambda(25\ \mu m)] > -0.3$ are H II regions but not AGB stars.

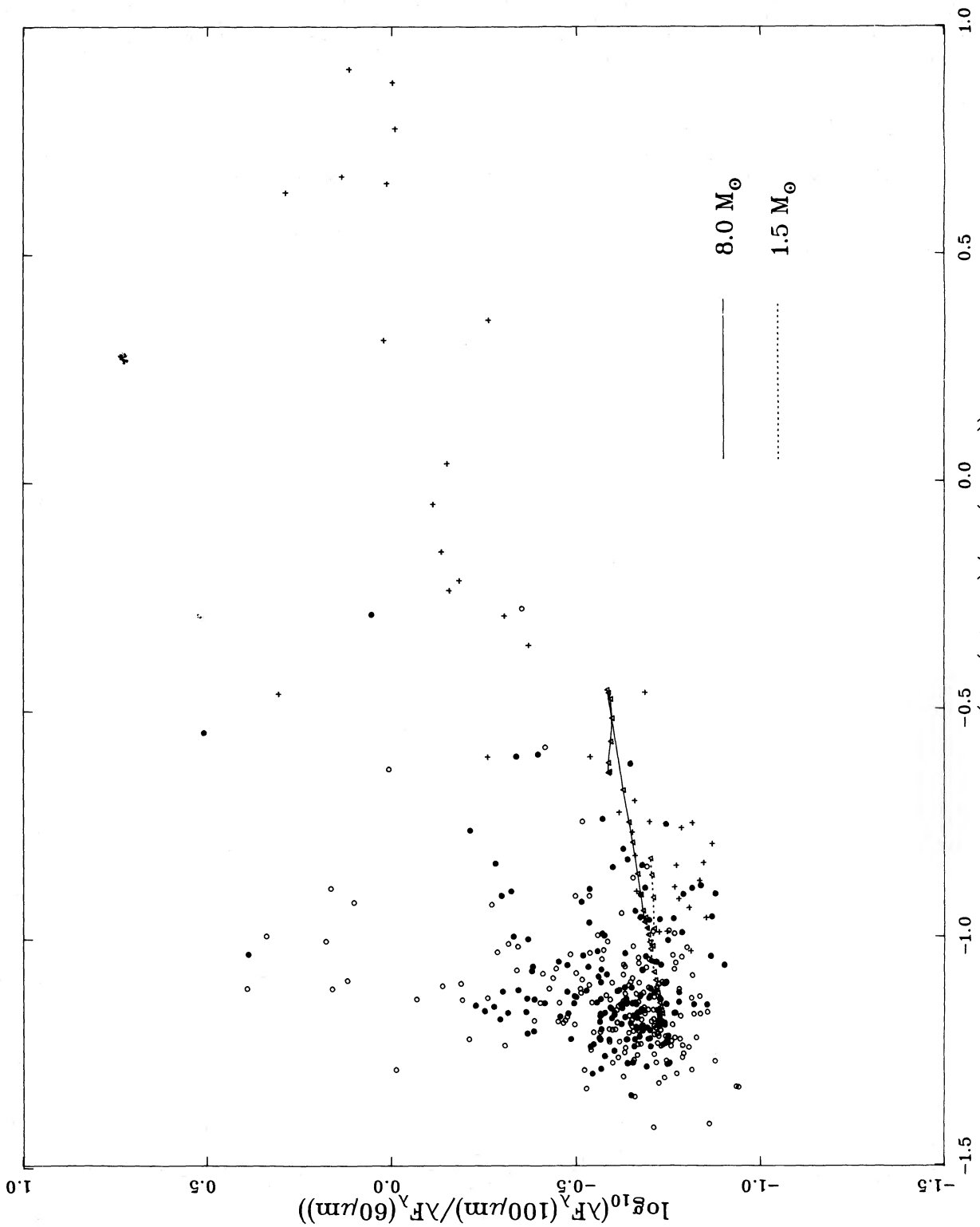

FIG. 13.—The evolutionary tracks on the 25/60/100 μm color-color diagram for AGB stars with initial masses 1.5 and 8 $M_\odot$. The symbols are the same as in Fig. 12. Note that most of the sources with $\log_{10}[\lambda F_\lambda(60\ \mu m)/\lambda F_\lambda(25\ \mu m)] > -0.3$ are H II regions but not AGB stars.

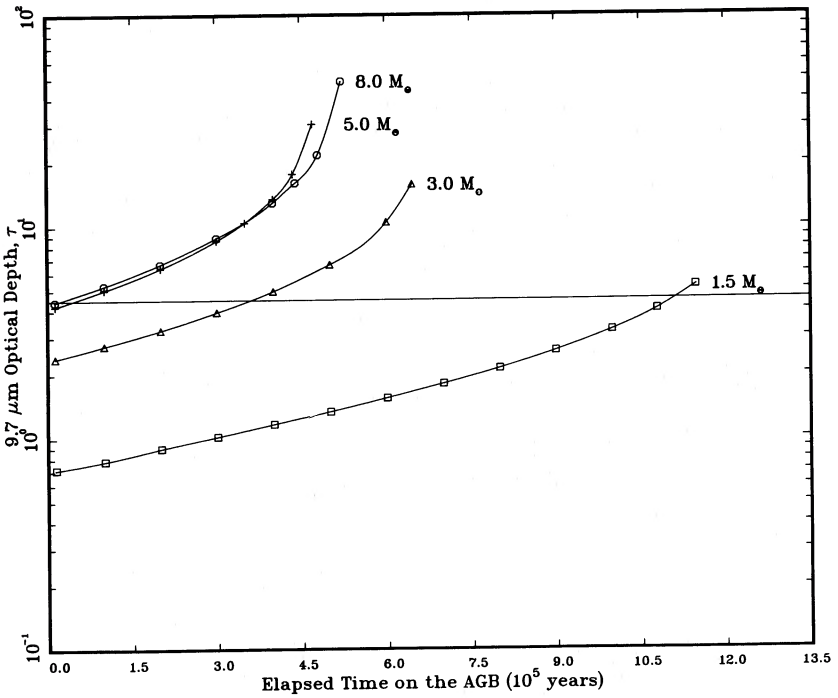

FIG. 14.—The time evolution of the 9.7 μm optical depth for stars with initial masses 1.5, 3, 5, and 8 $M_\odot$. The symbols on each curve indicate the positions where a model has been calculated.

the amount of cool dust available for self-absorption is larger. For example, for a condensation temperature of 1000 K, the transition optical depth decreases from 4 to 3.

VI. DISCUSSION

The above calculations present for the first time a self-consistent model of the AGB evolution. Since most of the stars on the late AGB have no optical counterparts, the only diagnostic of their evolutionary status is through the circumstellar spectra. By assuming a mass-loss formula, we are able to predict the evolution of the circumstellar spectrum throughout the entire AGB phase. The large range (3 orders of magnitude) of optical depths in the circumstellar ennvelopes of AGB stars imposes serious constraints on the type of mass-loss formulae allowed and the above model calculations show one mass-loss formula which is reasonably successful in explaining the observations. We will now discuss some of the implications of the above model.

a) The Mass-Loss Formula

If AGB stars indeed evolve from being emission objects to absorption objects along the band in the color-color diagram, then there must be a monotonic increase of $\dot{M}$ with time. The mass-loss formula used in the present model assumes that the mass-loss rate is proportional to the initial mass. This formula is clearly not the only one which can satisfy all the observational constraints. One can imagine a more complicated formula in which a low-mass star loses mass very rapidly near the end of the AGB and moves up the color-color diagram in a very short period of time and becomes an absorption object. With such a formula, there will be more overlap between the evolutionary tracks of stars of different initial masses on the color-color diagram than as given in Figure 10.

It will be difficult to separate the effects of age and initial mass because stars of different initial masses pass over the same point on the H-R diagram. As a result we do not wish to overplay the importance of the mass-loss formula in equation (18). While a definitive mass-loss formula is unlikely to emerge in the near future, it should be emphasized that the model calculations presented here allow for the first time a critical test of any empirical mass-loss formula.

b) A Superwind

A "superwind" has been postulated to bring down the envelope mass of AGB stars near the end of the AGB phase (Renzini 1983). In our model, the mass-loss rate is high (in comparison to the Reimers formula of eq. [17]) throughout the AGB phase and the postulation of a "superwind" is not necessary. We find that a gradual increase in mass-loss rate is in fact more consistent with the infrared and radio observations of mass loss of AGB stars. Since the mass-loss rate certainly increases with luminosity (or time on the AGB), one might wish to refer to the very last stage ($< 10^4$ yr) of mass loss as a "superwind" phase, although the distinction is strictly semantic. It would be wrong to refer to the OH/IR phase as the "superwind" phase because the late AGB, which coincides with the observation of OH/IR stars with no optical counterparts, certainly lasts more than 10^5 yr. Our models (e.g., Fig 10*d*) shows that a mass-loss rate of few times 10^{-6} yr^{-1} will completely obscure the photosphere of the star and such mass-loss rates cannot be in any sense considered "super."

c) Effects of Interstellar Extinction

One of the starting assumptions of this model is that the variation in the strength of the silicate feature from emission to absorption is the result of mass loss and evolution. It can be argued that the absorption features could be affected by interstellar absorption and the feature strength is only partly circumstellar. Using the same LRS sample as in this paper, Volk and Kwok (1987) show that interstellar extinction cannot

produce the large absorption features in class 30 objects and at the same time explain their *IRAS* photometric colors. Since the objects in our working sample are limited to nearby (<3 kpc) objects, the effect of extinction at 10 μm would be very small if a standard value for A_v of 2 mag per kpc is assumed.

If interstellar absorption is important then its effects should be observable in other stars in the LRSC. Many carbon stars lie in the plane but none is known to show the silicate feature in absorption. On the contrary, there are many sources in the plane which show the 10 μm feature in strong emission, unaffected by interstellar absorption. There are a few main-sequence stars (e.g., 05307+4105) that seem to have suffered from interstellar absorption at 10 μm, but their continuum color are so blue that they are never detected at 100 μm and consequently will not be part of our working sample.

More importantly, a star which is reddened by interstellar extinction alone has colors very different from the circumstellar model results presented here. In fact, our test models show that it is extremely difficult to reproduce the spectral behavior (the silicate absorption feature and the underlying continuum) of class 30 sources without significant optical depth in the circumstellar envelope. For these reasons, we conclude that the effect on the spectra used in our working sample due to interstellar extinction is minimal.

One of the problems of understanding the nature of OH/IR stars is the uncertainty in distance. Baud *et al.* (1985) have studied a number of OH/IR stars near the galactic bulge where the distance can be assumed to be known. Two OH/IR stars (OH 4.6−0.4 and OH 0.2+0.0) are found to have strong silicate absorption features. Using a distance of 10 kpc for the bulge, the luminosity of these two objects are estimated by Baud *et al.* to be $2.1 \pm 0.5 \times 10^4$ and $0.2 \pm 0.1 \times 10^4\ L_\odot$, respectively. The low luminosity of OH 0.2+0.0 suggests that it is likely to be a low-mass star. The presence of the absorption feature in OH 2.0+0.0 is therefore incompatable with the results of this paper. Two explanations may be offered to this problem. Baud *et al.* (1985) have considered that the absorption feature is interstellar but do not favor it. An alternative explanation is that the bulge stars have higher metallicity and therefore have higher dust optical depths in the circumstellar envelope. Recent observational results have indicated that stars in the bulge are metal-rich (Frogel and Whitford 1987), and our model may not be applicable to stars in the bulge.

e) *Population Statistics*

If the silicate feature in emission or absorption indeed reflects the initial mass of the AGB star as suggested above, then the number of observable emission objects can be predicted by convolving the length of the emission phase for star of each mass range with the initial mass function (IMF). Assuming the Salpeter IMF with the form $N(m) \propto m^{-2.35}$, we estimate a ratio of ~2.7 for emission to absorption objects, including the effect of luminosity bias. In comparison, the ratio of emission (class 20) to absorption (class 30) objects is 7.5 in the whole LRSC. In view of the many uncertainties in the basic parameters which go into this estimate this order of magnitude agreement is acceptable. Better agreement would be obtained if the IMF is steeper at high mass than in the Salpeter function. Alternatively if the constant in equation (17) increases more steeply with mass than the linear relation assumed here, there will be proportionally more stars have low mass-loss rates and the above ratio would also increase.

The above prediction can also be compared with the galactic distribution of the emission and absorption objects. As shown in Figures 4 and 5, the class 30 (absorption) objects are much more confined to the plane than the class 20 (emission) objects. While this can in part be attributed to absorption objects being more evolved on the AGB with a higher intrinsic luminosity and therefore are observable at larger distances, the difference in galactic distribution between the two populations may also be due to differences in progenitor masses as suggested by the model.

VII. CONCLUSIONS

We have performed time-dependent radiative transfer calculations for the circumstellar dust emission from AGB stars. The evolution of the infrared spectrum of the star is followed from a stellar evolution model based on one simple mass-loss formula. The model parameters are chosen such that the model emergent spectra to best approximate the low resolution spectra of AGB stars obtained by the *IRAS* satellite. A new dust opacity function is also derived from such a comparison. We find that the 10 μm silicate feature changes from emission to absorption at $\tau \sim 4$ and for sources with the deepest absorption features, the optical depth of the circumstellar envelope exceeds 500 at 10 μm.

The evolutionary tracks obtained from these models have also been able to reproduce the distribution of AGB and late-AGB stars on the color-color diagram. While the mass-loss formula used in the present calculations is probably not unique, the agreement between the model and *IRAS* photometric and spectroscopic observations is remarkable. Our calculations therefore represent the first quantitative test of mass-loss formulae for AGB stars. We believe that time-dependent models of this kind is an important step in the study of the poorly understood late-AGB and the models will have significant implications on the subsequent evolution to the planetary nebulae stage.

We thank C. M. Leung for providing us with the computer code DUSTCD used in this work. Miss Charlene Heisler assisted in the conversion of the code to the CYBER computer. We wish to thank H. J. Habing for helpful dscussions. The *IRAS* catalogs were supplied by the World Data Center in Greenbelt, Maryland. This work is supported by a grant to S. K. from the Natural Sciences and Engineering research Council of Canada.

APPENDIX

THE EXPONENTIAL MASS-LOSS FORMULA

It has been shown that if the mass-loss rate is a simple function stellar luminosity, then evolution on the AGB can be expressed in a closed analytical form (Kwok 1985). For example, if

$$\dot{M} = BL_*^{\beta}, \tag{A1}$$

TABLE 1

MASS-LOSS RATES PREDICTED BY THE EXPONENTIAL MASS-LOSS FORMULA

	$\beta = 1$		$\beta = 2$	
	$B = 1.91 \times 10^{-10}$	$M_\odot\ \mathrm{yr}^{-1}\ L_\odot^{-1}$	$B = 4.84 \times 10^{-15}$	$M_\odot\ \mathrm{yr}^{-1}\ L_\odot^{-1}$
$M_*(0)$ $M_\odot$	$\dot{M}(0)$ $(M_\odot\ \mathrm{yr}^{-1})$	$\dot{M}(T)$	$\dot{M}(0)$ $(M_\odot\ \mathrm{yr}^{-1})$	$\dot{M}(T)$
1.5.....	3.27 (−7)	5.84 (−7)	1.40 (−8)	2.04 (−7)
2.0.....	6.25 (−7)	1.18 (−6)	5.18 (−8)	6.50 (−7)
3.0.....	1.22 (−6)	2.42 (−6)	1.98 (−7)	1.93 (−6)
4.0.....	1.82 (−6)	3.86 (−6)	4.38 (−7)	3.50 (−6)
5.0.....	2.41 (−6)	5.16 (−6)	7.72 (−7)	5.25 (−6)
6.0.....	3.01 (−6)	6.54 (−6)	1.20 (−6)	7.15 (−6)
7.0.....	3.60 (−6)	7.88 (−6)	1.72 (−6)	9.18 (−6)
8.0.....	4.20 (−6)	9.15 (−6)	2.34 (−6)	1.13 (−5)

then

$$M_c(t) = (1 - e^{t/t_0})M_0 + M_c(0)e^{t/t_0} \tag{A2}$$

$$\dot{M}(t) = \dot{M}_0\, e^{\beta t/t_0} \tag{A3}$$

$$M_*(t) = M_*(0) - [\dot{M}_0\, t_0/\beta](e^{\beta t/t_0} - 1)\,, \tag{A4}$$

where

$$\dot{M}_0 = B\{L_0[M_c(0) - M_0]\}^\beta \tag{A5}$$

is the mass-loss rate at $t = 0$ and is dependent on the mass of the star. In this formula, the mass-loss rate grows exponentially with time.

With an analytical solution, the constant $\dot{M}_0$ can be determined from the maximum white dwarf progenitor mass ($M_{\rm wd}$). For example, if $M_{\rm wd} = 8\ M_\odot$, then the lifetime (T) of the AGB can be found by setting $M_c(t) = 1.41\ M_\odot$ and solving equation (A2). Substituting T into equation (A4) with $M_*(T) = 1.41\ M_\odot$ then gives the value of $\dot{M}_0$ for a $8\ M_\odot$ star. Using the values of $M_c(0)$ of Iben (1981), the values of $\dot{M}_0$ can be calculated as a function of β and M_*. The values of $\dot{M}_0$ and the mass-loss rates at $t = 0$ and $t = T$ for two values of β are given in Table 1.

Table 1 shows that the exponential mass-loss formula gives $\dot{M}$ values from $3 \times 10^{-7}\ M_\odot\ \mathrm{yr}^{-1}$ up to $9 \times 10^{-6}\ M_\odot\ \mathrm{yr}^{-1}$ for $\beta = 1$, and a slightly larger range for $\beta = 2$. This range of mass loss is less than the observed range of values (Knapp *et al.* 1982) and is not wide enough to account for the large change in 10 μm optical depths observed in AGB stars. Specifically, this mass-loss formula fails to reproduce the deep silicate absorption features common among late-AGB stars (Kwok, Hrivnak, and Boreiko 1987). If the dust-to-gas ratio is increased to produce absorption feature objects then the evolutionary tracks do not give enough coverage of the part of the color-color diagram occupied by the class 20 objects. We therefore conclude that the mass-loss formula of equation (A1) is not as successful as equation (18) in explaining the behavior of AGB stars.

REFERENCES

Baud, B., Habing, H. J., Matthews, H. E., and Winnberg, A. 1979, *Astr. Ap. Suppl.*, **35**, 179.
Bedijn, P. 1986, in *Light on Dark Matter*, ed. F. P. Israel (Dordrecht: Reidel), p. 119.
———. 1987, preprint.
Biermann, P., and Harwit, M. 1980, *Ap. J. (Letters)*, **241**, L105.
Chan, S. J., and Kwok, S. 1988, submitted to *Ap. J.*
Crabtree, D. R., and Martin, P. G. 1979, *Ap. J.*, **227**, 900.
Engels, D., Kreysa, E., Shultz, G. V., and Sherwood, W. A. 1983, *Astr. Ap.*, **124**, 123.
Feast, M. 1986, in *Light on Dark Matter*, ed. F. P. Israel (Dordrecht: Reidel), p. 339.
Frogel, J. A., and Whitford, A. E. 1987, *Ap. J.*, **320**, 199.
Gehrz, R. D., and Woolf, N. J. 1971, *Ap. J.*, **165**, 285.
Gilman, R. C. 1969, *Ap. J. (Letters)*, **155**, L185.
Habing, H. J., Olnon, F. M., Chester, T., Gillett, F., Rowan-Robinson, M., and Neugebauer, G. 1985, *Astr. Ap.*, **152**, L1.
Herman, J., and Habing, H. J. 1985, *Astr. Ap. Suppl.*, **59**, 523.
Iben, I. 1981, *Ap. J.*, **246**, 278.
Iben, I., and Renzini, A. 1983, *Ann. Rev. Astr. Ap.*, **21**, 271.
IRAS Catalogs and Atlases, Explanatory Supplement. 1985, ed. C. A. Beichman, G. Neugebauer, H. J. Habing, P. E. Clegg, and T. J. Chester (Washington D.C.: US Government Printing Office).
IRAS Catalogs and Atlases, Catalog of Low Resolution Spectra. 1986, *Astr. Ap. Suppl.*, **65**, (LRSC).
Johansson, L. E. B., Anderson, C., Goss, M. W., and Winnberg, A. 1977, *Astr. Ap. Suppl.*, **28**, 199.
Jones, T. J. 1987, in *The Late Stages of Stellar Evolution*, ed. S. Kwok and S. R. Pottasch (Dordrecht: Reidel), p. 3.
Jones, T., and Merrill, K. M. 1976, *Ap. J.*, **209**, 509.
Knapp, G., Phillips, T. G., Leighton, R. B., Lo, K. Y., Wannier, P. G., and Wootten, H. A. 1982, *Ap. J.*, **252**, 616.
Kwok, S. 1975, *Ap. J.*, **198**, 583.
———. 1985, in *Relations between Chromospheric-Coronal Heating and Mass Loss in Stars*, ed. J. Zirker (Trieste: Osservatorio Astronomico), p. 188.
———. 1987, *Phys. Rep.*, in press.
Kwok, S., Hrivnak, B. J., and Boreiko, R. T. 1987, *Ap. J.*, **321**, 975.
Leung, C. M. 1975, *Ap. J.*, **199**, 340.
———. 1976, *Ap. J.*, **209**, 75.
Merrill, K. M. 1977, in *IAU Colloquium 42, The Interaction of Variable Stars with Their Environment*, ed. R. Kippenhahn, J. Rahe, and W. Strohmeier, (*Veröff. Remeis-Sterw. Bamberg*, Vol. **11**, No. 121), p. 446.
Merrill, K. M., and Stein, W. A. 1976, *Pub. A.S.P.*, **88**, 874.
Neugebauer, G., and Leighton, R. B. 1969, *Two Micron Sky Survey* (NASA SP-3047) (Washington: NASA).
Olnon, F. M., Baud, B., Habing, H. J., deJong, T., and Pottasch, S. R. 1984, *Ap. J. (Letters)*, **278**, L41.
Ostlie, D. A., Cox, A. N., and Cahn, J. H. 1982, in *Pulsation in Classical and Cataclysmic Variable Stars*, ed. J. P. Cox and C. J. Hansen (University of Colorado Press), p. 297.
Pacynski, B. 1971, *Acta Astr.*, **31**, 417.
Pouw, A. 1983, *British Interplanetary Soc.*, **36**, 17.
Reimers, X. X. 1975, *Mém. Soc. Roy. Sci. Liège 6th Ser.*, **8**, p. 369.
Renzini, A. 1983, in *IAU Symposium 103, Planetary Nebulae*, ed. R. D. Flower (Dordrecht: Reidel), p. 267.
Rowan-Robinson, M., and Harris, S. 1983*a*, *M.N.R.A.S.*, **202**, 767.
——— 1983*b*, *M.N.R.A.S.*, **202**, 797.
Spagna, G. F., and Leung, C. M. 1983, *Comp. Phys. Comm.*, **28**, 337.

Tamm. R. E., and Schwartz, R. D. 1976, *Ap. J.*, **204**, 842.
Volk, K., and Kwok, S. 1987, *Ap. J.*, **315**, 654.
———. 1988, in preparation.
Walker, R. G., and Price, S. D. 1975, *AFCRL Infrared Sky Survey*, Vol. **1**, AFCRL-Tr-75-0373.
Weidemann, V., and Koester, D. 1983, *Astr. Ap.*, **121**, 77.
Wood, P. R., and Cahn, J. H. 1977, *Ap. J.*, **211**, 499.
Woolf, N. J., and Ney, E. P. 1969, *Ap. J. (Letters)*, **155**, L181.

SUN KWOK: Department of Physics, The University of Calgary, Calgary, Alberta, Canada T2N 1N4

K. M. VOLK: Mail Stop N245-6 NASA Ames Research Center, Moffett Field, CA 94035